RESEARCH ARTICLE

Key Points:
- A machine learning potential of ab initio quality has been developed for hydrous $MgSiO_3$ system
- Hydrogen diffusion is sluggish in both bridgmanite and post-perovskite, leading to heterogeneous water distribution in the lower mantle
- Proton diffusion may be associated with the variation of electrical conductivity in the deep mantle

Correspondence to:

Y. Peng and J. Deng,
yhpeng@princeton.edu;
jie.deng@princeton.edu

Author Contributions:

Conceptualization: Jie Deng
Data curation: Yihang Peng
Formal analysis: Yihang Peng
Investigation: Yihang Peng
Methodology: Yihang Peng, Jie Deng
Project administration: Jie Deng
Software: Yihang Peng, Jie Deng
Supervision: Jie Deng
Visualization: Yihang Peng
Writing – original draft: Yihang Peng
Writing – review & editing: Jie Deng

Hydrogen Diffusion in the Lower Mantle Revealed by Machine Learning Potentials

Yihang Peng[1] and Jie Deng[1]

[1]Department of Geosciences, Princeton University, Princeton, NJ, USA

Abstract Hydrogen may be incorporated into nominally anhydrous minerals including bridgmanite and post-perovskite as defects, making the Earth's deep mantle a potentially significant water reservoir. The diffusion of hydrogen and its contribution to the electrical conductivity in the lower mantle are rarely explored and remain largely unconstrained. Here we calculate hydrogen diffusivity in hydrous bridgmanite and post-perovskite, using molecular dynamics simulations driven by machine learning potentials of ab initio quality. Our findings reveal that hydrogen diffusivity significantly increases with increasing temperature and decreasing pressure, and is considerably sensitive to hydrogen incorporation mechanism. Among the four defect mechanisms examined, $(Mg + 2H)_{Si}$ and $(Al + H)_{Si}$ show similar patterns and yield the highest hydrogen diffusivity. Hydrogen diffusion is generally faster in post-perovskite than in bridgmanite, and these two phases exhibit distinct diffusion anisotropies. Overall, hydrogen diffusion is slow on geological time scales and may result in heterogeneous water distribution in the lower mantle. Additionally, the proton conductivity of bridgmanite for $(Mg + 2H)_{Si}$ and $(Al + H)_{Si}$ defects aligns with the same order of magnitude of lower mantle conductivity, suggesting that the water distribution in the lower mantle may be inferred by examining the heterogeneity of electrical conductivity.

Plain Language Summary Water or hydrogen may be trapped in the Earth's deep mantle, affecting the state and evolution of our planet. However, the mobility of hydrogen in the lower mantle remains poorly understood. By using advanced machine learning-driven simulations, we find that hydrogen in lower-mantle silicates diffuses faster at higher temperatures and lower pressures, and how hydrogen is incorporated into the silicates greatly influences this mobility. Two specific ways of hydrogen incorporation were found to allow hydrogen to move very efficiently. On a geological scale, the transport of hydrogen is slow, suggesting that water may be unevenly distributed in the Earth's lower mantle. The electrical conductivity associated with the movement of hydrogen aligns with previous observations of the Earth's mantle. Variations in electrical conductivity in the lower mantle may inform where water is located in the Earth's deep interior.

1. Introduction

Water is widely present in the Earth's deep interior (Ohtani, 2021), and affects the physical and chemical properties of the Earth's materials, including rheology (Karato et al., 1986), seismic wave velocities (Karato, 1995), phase transitions (Ohtani & Litasov, 2006), and electrical conductivity (Karato, 1990). Therefore, investigating the behavior of hydrogen in mantle phases is important for understanding the dynamics and evolution of the Earth. $(Mg,Fe)SiO_3$ bridgmanite (Brg) is believed to be the dominant phase in the Earth's lower mantle. This material remains stable across a broad range of depths, from 660 km discontinuity down to the bottom of the mantle, where the pressure and temperature (P/T) conditions may change from ~23 GPa and 2,000 K to ~136 GPa and 4,000 K (Fiquet et al., 2010). Bridgmanite may transform into post-perovskite (pPv) at the lowermost mantle conditions (above 125 GPa and 2,500 K, Murakami et al., 2004). Water or hydrogen can be incorporated into bridgmanite and post-perovskite as defects (Fu et al., 2019; Townsend et al., 2016), potentially forming volatile-rich reservoirs in the lower mantle (Hallis et al., 2015). The water storage capacity in the lower mantle is still under debate, since studies on the water solubility in bridgmanite have not reached a consensus. As summarized by Lu and Li (2023), experimental results show water content in bridgmanite spanning over three orders of magnitude. Even the most recent studies have yielded results ranging from less than 100 ppm (Ishii et al., 2022; Liu et al., 2021) to over 1,000 ppm (Fu et al., 2019; Y.-N. Yang et al., 2023). The solubility of water in bridgmanite is potentially influenced by a combination of factors including chemical composition, pressure, temperature, and oxygen fugacity, and is likely to have a strong depth dependence (Lu & Li, 2023; Muir & Brodholt, 2018; Y.-N. Yang et al., 2023).

Owing to its light atomic weight and small radius, hydrogen may be highly mobile and characterized with large diffusivity. The possible incorporation of hydrogen into bridgmanite and post-perovskite and its presumably large diffusivity may affect the geophysical and geochemical properties of the deep mantle, including electrical conductivity.

Electrical conductivity of the Earth's lower mantle exhibits significant variations both radially and laterally revealed by geomagnetic observations (e.g., Khan et al., 2011; Olsen, 1999b; Tarits & Mandea, 2010; Verhoeven et al., 2021). Using three-dimensional electromagnetic inversion, Tarits and Mandea (2010) reported a laterally heterogeneous conductivity structure at the depth range of 900–1,400 km. In addition, with resolution limited to the depth range of ~500–1,200 km, Khan et al. (2011) found lateral variations in electrical conductivity throughout the mantle, and the magnitude of the variation reaches 1 S m^{-1}. Yet, the source of these heterogeneities remains enigmatic. The electrical conductivity of the lower mantle is sensitive to the presence of a trace amount of hydrogen due to its high mobility (Karato, 1990). Consequently, the heterogeneous electrical conductivity may be caused by the heterogeneous distribution of water (Hae et al., 2006; Ohtani, 2021; Sun et al., 2015; Zhou et al., 2022). Assessing this hypothesis requires a thorough understanding of hydrogen diffusivity in bridgmanite and post-perovskite, as both the distribution of water in the lower mantle and hydrogen's contribution to electrical conductivity are governed by the diffusion of hydrogen. However, neither theoretical nor experimental data of hydrogen diffusivity in bridgmanite or post-perovskite are currently available.

In this study, we perform molecular dynamics (MD) simulations to investigate the hydrogen diffusion in bridgmanite and post-perovskite. Calculating diffusivity using ab initio molecular dynamics (AIMD) simulations is straightforward and well-developed, with no ad hoc diffusion pathway assumed. In these simulations, atoms move in a periodic box driven by Newtonian dynamics, with interatomic forces computed by the density functional theory (DFT), and diffusivity is directly derived from trajectories of atoms. Deriving a statistically robust result, however, is very costly, especially when the diffusion of atoms is sluggish (e.g., Caracas & Panero, 2017). Moreover, a system composed of thousands of atoms or even tens of thousands of atoms is required to simulate bridgmanite and post-perovskite with realistic water contents of less than thousands of ppm, which exceeds the capacity of ab initio methods, where computational cost scales to the third or fourth power of the number of electrons.

Machine learning potentials (MLPs) are an emerging method allowing to simulating large systems and long simulation trajectories with high efficiency (the cost scales linearly with the number of atoms) while maintaining ab initio accuracy (Zhang et al., 2018). MLPs have recently proven successful in accurately capturing various crystal defect properties, including their kinetics (Freitas & Cao, 2022). Our MLP for water-bearing bridgmanite and post-perovskite is developed by training an artificial neural network model with the ab initio data, following the protocol described in Deng et al. (2023a). Trained with atomic coordinates, energies, stresses, and atomic forces from AIMD simulations, the model can predict potential energy and force field based on the local environment of atoms, which are further used to perform MD simulations. The long trajectories and large systems made possible by the MLP facilitate a detailed examination of hydrogen diffusion under wide pressure, temperature, and compositional conditions. The results inform the distribution of water in the lower mantle and the contributions of hydrogen to the electrical conductivity of bridgmanite and post-perovskite, which are further compared against geophysical observations.

2. Methods

2.1. Building a Machine Learning Potential

We adopt the DeePMD approach (Wang et al., 2018; Zhang et al., 2018) to build an MLP from ab initio data. In this approach, the total potential energy is written as the sum of the energy of each atom, $E = \sum_{i=1}^{N} E_i = \sum_{i=1}^{N} \epsilon(\chi_i)$, where N is the total number of atoms, E_i is the contribution to the total energy from atom i, and χ_i is a descriptor representing the local atomic environment and is a function of the coordinates of the atoms in the vicinity of atom i.

In this study, the descriptor is parameterized using an embedding network with three hidden layers of 25, 50, and 100 nodes, and the form of the potential energy surface is determined using a three-layer fitting network with 240 nodes in each layer. The atomic local environment is described with a cutoff radius of 6 Å. The loss function is defined as

$$L\left(p_\epsilon, p_f, p_\xi\right) = p_\epsilon \Delta \epsilon^2 + \frac{p_f}{3N}\sum_i |\Delta \mathbf{F}_i| + \frac{p_\xi}{9}\|\Delta \xi\|^2 \tag{1}$$

where p_ϵ, p_f, p_ξ are tunable prefactors for the difference between the MLP prediction and training data. Here ϵ is the energy per atom, $\mathbf{F}_i$ is the atomic force of atom i, ξ is the virial tensor divided by N, and N is the number of atoms. We follow Deng et al. (2023a) to increase both p_ϵ and p_ξ from 0.02 to 1 while decreasing p_f from 1,000 to 1 over the course of training.

Our MLP is built upon an earlier version for pure $MgSiO_3$ (Deng et al., 2023a). This new MLP targets a wider compositional space, covering not only pure $MgSiO_3$, but also pure H_2O, pure H_2 (liquid only), and intermediate compositions with bulk compositions of $aMgSiO_3 + bH_2O$, $aMgSiO_3 + bH_2$ and of $aMgSiO_3 + cOH$, where $a = 27$ or 32, $b = 1$ to 9, $c = 1$ to 18. In addition, we explicitly consider the intermediate composition obtained by charge-coupled cation substitution, that is, $aMgSiO_3 + bH - cMg$, where $a = 32$, $b = 2c$, corresponding to $(2H)_{Mg}$; $aMgSiO_3 + bH - cSi$, where $a = 32$, $b = 4c$, corresponding to $(4H)_{Si}$; $aMgSiO_3 + bH + cMg - dSi$, where $a = 32$, $b + 2c = 4d$, corresponding to $(Mg + 2H)_{Si}$.

For all compositions, we employ an iterative training scheme proposed by Deng et al. (2023a) to ensure that the potential energy surface is sufficiently sampled. This scheme mainly entails enhanced sampling using LAMMPS (Plimpton, 1995) interfaced with PLUMED 2 (Tribello et al., 2014), principal component analysis on the MD trajectories with the farthest point sampling technique (Cheng et al., 2020; Imbalzano et al., 2018), recalculation with DFT at higher accuracy for selected frames, and refining the MLP with recalculated new frames. The iterative training scheme ensures that the training set is succinct and balanced. Indeed, the size of the final training set is very small, consisting of only 9095 configurations. Here, a "configuration" refers to a unique spatial arrangement of atoms, labeled with ab initio energy and atomic forces for training the MLP. This training set is relatively small but covers a wide range of temperature and pressure (1,000–8,000 K and 0–220 GPa), compared to typically tens of thousands of frames for mono-atomic species over much narrower ranges of pressure and temperature conditions (Niu et al., 2020; M. Yang et al., 2021). The electronic temperatures are taken into account during both the DFT calculation and the MLP training processes. To mitigate edge effects during machine learning, we deliberately encompass a pressure range significantly exceeding the highest pressure found in Earth's mantle. This approach ensures robustness. For instance, when the input data covers solely the 0–140 GPa pressure range, the MLP's performance might be compromised, particularly at the core-mantle boundary conditions. We note that our training set includes a significant number of frames that sample various defects and interfaces, thanks to the multithermal-multibaric technique used (Deng et al., 2023a; Piaggi & Parrinello, 2019). As such, though not the focus of this study, our MLP can also be useful for studying the phase transition of the (hydrous) $MgSiO_3$ system, as well as other transport properties including thermal conductivity (Peng & Deng, 2024).

2.2. ab initio Molecular Dynamics Simulations

To train the MLP, we perform AIMD simulations on pure and hydrous $MgSiO_3$, as well as pure H_2 and H_2O based on DFT under periodic boundary conditions. We adopt the PBEsol approximation (Perdew et al., 2008) using VASP (Kresse & Furthmuller, 1996) with the projector augmented wave method (Kresse & Joubert, 1999). The physical properties of silicates and oxides calculated using the PBEsol approximation are consistent with experimental data (Deng & Stixrude, 2021a; Scipioni et al., 2017). The core radii of O ($2s^2 2p^4$), Si ($3s^2 3p^2$), Mg ($2p^6 3s^2$), and H ($1s^1$) are 0.820 Å, 1.312 Å, 1.058 Å, and 0.370 Å, respectively. AIMD simulations are performed in the canonical ensemble with a fixed number of atoms, volume, and temperature, controlled by the Nosé-Hoover thermostat (Hoover, 1985). Our AIMD simulations run for 5–20 ps with a time step of 1 fs. The Mermin functional is used to presume that ions and electrons reach thermal equilibrium (Mermin, 1965). For the initial data set, we employ a 500-eV energy cutoff for AIMD simulations and sample the Brillouin zone at the Γ point. The energy, force, and stress of selected configurations for building the MLP are recalculated at higher precision with the following changes. The energy cutoff is increased from 500 to 800 eV, the precision for finding the self-consistent solution to the Kohn-Sham equations is increased from 10^{-4} eV to 10^{-6} eV, and sampling of the Brillouin zone is increased from the Γ point only to a $2 \times 2 \times 2$ Monkhorst-Pack mesh. We emphasize that this high-accuracy recalculation is crucial for enhancing the precision and scope of the MLP (Deng & Stixrude, 2021b).

2.3. Molecular Dynamics Simulations Driven by Machine Learning Potentials

Hydrogen may be incorporated into nominally anhydrous minerals as Si or Mg vacancies through charge-coupled substitution mechanisms. We introduce hydrogen defects by substituting Mg and Si with H while maintaining charge balance. For the $MgSiO_3$ system, we explore three representative hydrogen incorporation mechanisms: $(2H)_{Mg}$, $(4H)_{Si}$, and $(Mg + 2H)_{Si}$, where the subscript indicates the lattice site of the defect, and inside the parentheses are atoms after substitution. These defects are also found in other mantle silicates such as wadsleyite and ringwoodite (Kudoh & Inoue, 1999; Panero et al., 2013). Muir and Brodholt (2018) present evidence that water is preferentially incorporated into bridgmanite as $(Al + H)_{Si}$ due to its high configurational entropy. It is worth noting that this defect shares some commonalities with the $(Mg + 2H)_{Si}$: both have a cation carrying a positive charge but less than that of Si, and achieve charge balance by supplementing protons. Given the possibility of $(Al + H)_{Si}$ being an energy-favorable defect, we employed ab initio calculations combined with the machine learning force field method using VASP to simulate the Al-bearing bridgmanite with $(Al + H)_{Si}$ defects. We observed that $(Al + H)_{Si}$ and $(Mg + 2H)_{Si}$ exhibit remarkably similar hydrogen diffusion patterns, with closely matching hydrogen diffusion coefficients. Our detailed methods and results for $(Al + H)_{Si}$ are presented in Text S1 in Supporting Information S1. Owing to the similarity in hydrogen diffusion between $(Al + H)_{Si}$ and $(Mg + 2H)_{Si}$, we propose that they can be treated analogously, and the following discussions about $(Mg + 2H)_{Si}$ might well apply to $(Al + H)_{Si}$ too.

We consider a range of supercells for $MgSiO_3$ bridgmanite and post-perovskite, containing 80 ($2 \times 2 \times 1$ for *Pbnm* bridgmanite and $4 \times 1 \times 1$ for *Cmcm* post-perovskite) to 81,920 ($16 \times 16 \times 16$ for *Pbnm* bridgmanite and $32 \times 8 \times 16$ for *Cmcm* post-perovskite) atoms. The largest supercell considered enables constructing systems with water content as low as 175 ppm. The distribution of water in the supercell is initially uniform, that is, all defects are evenly distributed in the supercell, except for the data in Figure 4, where the defect sites are randomly selected. We carefully study the relative stability of configurations with random defect distributions and their impact on the hydrogen diffusion coefficient, concluding that while defect distribution marginally affects diffusion anisotropy, it has minimal impact on the bulk diffusivity. The computational details are provided in Text S2 in Supporting Information S1.

MD simulations are performed using LAMMPS (Plimpton, 1995) and DeePMD-kit (Wang et al., 2018) under periodic boundary conditions. For each defect mechanism, we consider three representative temperatures (2,000, 3,000, and 4000 K) and three pressures (25, 75, and 140 GPa), covering the P/T conditions of the entire lower mantle. Additionally, we conduct simulations along an adiabatic geotherm (Katsura et al., 2010), ranging from 700 to 2,900 km in depth. Detailed simulation setups can be found in Table S1 and Table S2. Initially, we relax systems under an isothermal-isobaric ensemble for 25 ps at target temperatures and pressures. The resulting configurations are then used for simulations under a canonical ensemble employing the Nosé-Hoover thermostat (Hoover, 1985), generating 1-ns trajectories from which hydrogen diffusivity is derived. The timestep of all simulations is 0.5 fs.

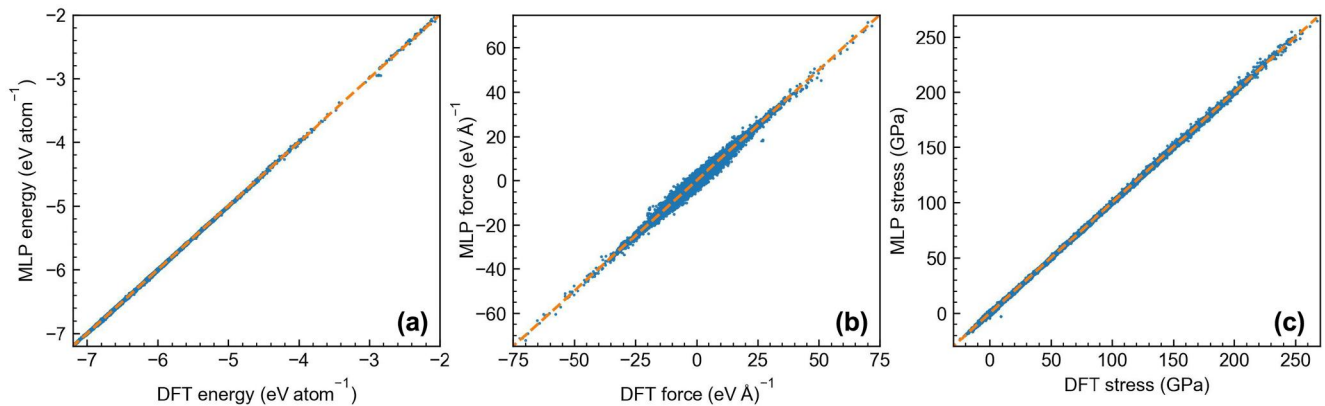### 2.4. Hydrogen Diffusion Coefficient and Proton Conductivity

Hydrogen diffusivity, D_H, is derived as the slope of mean square displacement (MSD) by,

$$D_{\mathrm{H}} = \lim_{t \to \infty} \frac{\mathrm{MSD}}{6t} = \lim_{t \to \infty} \frac{\left\langle \left[\vec{r}(t + t_0) - \vec{r}(t_0) \right]^2 \right\rangle_{\mathrm{H}}}{6t} \tag{2}$$

where $\vec{r}(t)$ is the particle trajectories continuous in Cartesian space, and $\langle \cdots \rangle_H$ represents an average over all hydrogen atoms and over time with different origins t_0 (Karki, 2015). Only when MSD is a linear function of time do we intercept the segment of MSD and calculate the diffusion coefficient by linear fitting (Figure S1 in Supporting Information S1). The diffusion coefficients as a function of temperature obtained from our simulations are fitted by the Arrhenius equation,

$$D = D_0 e^{-\frac{\Delta H}{RT}} \tag{3}$$

where D_0 is the pre-exponential factor, R is the ideal gas constant, T is the temperature in Kelvin, and ΔH is the activation enthalpy.

Figure 1. Comparisons of energies (a), atomic forces (b), and stresses (c) between density functional theory and the machine learning potential for all the test data (50,587 configurations) at temperatures ranging from 1,000 to 8,000 K and pressures from ∼0 GPa–220 GPa. 50,587 energies, 49,422,324 force components, and 910,566 stress components are included in these comparisons. The orange dashed lines are guides for perfect matches.

The hydrogen diffusion coefficient and the proton conductivity σ_H, that is, the electrical conductivity (unit: S m^{-1}) contributed by hydrogen diffusion, are related by the Nernst-Einstein equation (Karato, 1990),

$$\sigma_H = \frac{F^2}{RT}c_H z^2 D \tag{4}$$

where F is the Faraday's constant in C mol^{-1}; c_H is the molar concentration of hydrogen in mol m^{-3}; z is the charge of the ion in C; and D is the hydrogen diffusion coefficient in m^2 s^{-1}. We use a nominal charge of $z = +1e$ for proton following previous literature (e.g., Hae et al., 2006; Novella et al., 2017; Sun et al., 2015). We perform a detailed analysis of the effective charge of hydrogen in Text S3 in Supporting Information S1.

3. Results

3.1. Benchmarks of the Machine Learning Potential

We compare the energies, atomic forces, and stresses from the MLP to those from DFT simulations for 50,587 configurations that are not included in the training set (Figure 1). The root-mean-square errors of the energies, atomic forces, and stresses are 6.39 meV atom^{-1}, 0.28 eV Å^{-1}, and 0.45 GPa, respectively. These uncertainties are comparable to the typical precision of AIMD simulations (Deng & Stixrude, 2021a).

To further validate the reliability of the MLP, we compare the MSD and hydrogen diffusivity obtained from ab initio calculations to that from our MLP (Figure S1 in Supporting Information S1). Figure S1b in Supporting Information S1 shows that the uncertainty in MSD significantly increases over time, since larger values of t in Equation 2 mean a smaller data set for averaging, resulting in larger statistical errors. Therefore, we chose to calculate the diffusion coefficient from the MSD over a short time segment ($t < 30$ ps). For the same initial condition, DFT and MLP methods yield nearly identical MSDs in the selected region. The discrepancy in the DFT and MLP results for $t > 30$ ps can be attributed to the significantly increased statistical error in MSD, and the mean values of MSD calculated from DFT and MLP methods still fall within the error bars of each other. As shown in Figure S1c in Supporting Information S1, hydrogen diffusivities derived from the two methods are highly consistent, indicating that our MLP has accuracy comparable to ab initio calculations in computing the diffusivity. We emphasize that in this example the simulation using MLP is approximately 5,000 times faster than that driven by DFT.

3.2. Convergence and Uncertainty of Hydrogen Diffusion Coefficient

To investigate the impact of system size on diffusivity, we construct a series of supercells of hydrous bridgmanite that contain 81 to 41,472 atoms, incorporating hydrogen via (2H)$_{Mg}$ mechanism. The results suggest that hydrogen diffusivities initially increase with system sizes before eventually converging to a constant. The positive

Table 1
Pre-Exponential Factor (D$_0$) and Activation Enthalpy (ΔH) of Hydrogen Diffusion in Bridgmanite (Brg) and Post-Perovskite (pPv) Fitted by the Arrhenius Equation

Defect	Pressure (GPa)	Mineral	Chemical composition	C_{water} (wt%)	ΔH (kJ mol^{-1})	$\log_{10}[D_0$ (m^{2}s^{-1})]
$(2H)_{Mg}$	25	Brg	$Mg_{16368}Si_{16384}O_{49152}H_{32}$	0.0175	174.5	−4.57
$(2H)_{Mg}$	25	Brg	$Mg_{8160}Si_{8192}O_{24576}H_{64}$	0.0702	212.5	−4.02
$(2H)_{Mg}$	25	Brg	$Mg_{8128}Si_{8192}O_{24576}H_{128}$	0.140	215.4	−4.00
$(2H)_{Mg}$	75	Brg	$Mg_{8128}Si_{8192}O_{24576}H_{128}$	0.140	250.1	−4.36
$(2H)_{Mg}$	140	Brg	$Mg_{8128}Si_{8192}O_{24576}H_{128}$	0.140	393.5	−2.96
$(2H)_{Mg}$	25	Brg	$Mg_{960}Si_{1024}O_{3072}H_{128}$	1.14	159.8	−5.19
$(2H)_{Mg}$	75	Brg	$Mg_{960}Si_{1024}O_{3072}H_{128}$	1.14	198.8	−5.25
$(2H)_{Mg}$	140	Brg	$Mg_{960}Si_{1024}O_{3072}H_{128}$	1.14	265.4	−4.65
$(4H)_{Si}$	25	Brg	$Mg_{8192}Si_{8160}O_{24576}H_{128}$	0.140	248.5	−3.70
$(4H)_{Si}$	75	Brg	$Mg_{8192}Si_{8160}O_{24576}H_{128}$	0.140	262.2	−4.48
$(4H)_{Si}$	140	Brg	$Mg_{8192}Si_{8160}O_{24576}H_{128}$	0.140	402.4	−3.07
$(4H)_{Si}$	25	Brg	$Mg_{1024}Si_{992}O_{3072}H_{128}$	1.13	163.5	−5.05
$(4H)_{Si}$	75	Brg	$Mg_{1024}Si_{992}O_{3072}H_{128}$	1.13	199.3	−5.07
$(4H)_{Si}$	140	Brg	$Mg_{1024}Si_{992}O_{3072}H_{128}$	1.13	197.5	−5.40
$(Mg + 2H)_{Si}$	25	Brg	$Mg_{8256}Si_{8128}O_{24576}H_{128}$	0.140	104.5	−5.59
$(Mg + 2H)_{Si}$	75	Brg	$Mg_{8256}Si_{8128}O_{24576}H_{128}$	0.140	136.6	−5.50
$(Mg + 2H)_{Si}$	140	Brg	$Mg_{8256}Si_{8128}O_{24576}H_{128}$	0.140	166.8	−5.39
$(Mg + 2H)_{Si}$	25	Brg	$Mg_{1088}Si_{960}O_{3072}H_{128}$	1.12	82.9	−5.92
$(Mg + 2H)_{Si}$	75	Brg	$Mg_{1088}Si_{960}O_{3072}H_{128}$	1.12	104.9	−5.88
$(Mg + 2H)_{Si}$	140	Brg	$Mg_{1088}Si_{960}O_{3072}H_{128}$	1.12	114.8	−6.01
$(2H)_{Mg}$	140	pPv	$Mg_{8128}Si_{8192}O_{24576}H_{128}$	0.140	239.2	−5.01
$(2H)_{Mg}$	140	pPv	$Mg_{960}Si_{1024}O_{3072}H_{128}$	1.14	256.1	−4.85
$(4H)_{Si}$	140	pPv	$Mg_{8192}Si_{8160}O_{24576}H_{128}$	0.140	376.7	−3.31
$(4H)_{Si}$	140	pPv	$Mg_{1024}Si_{992}O_{3072}H_{128}$	1.13	182.9	−5.61
$(Mg + 2H)_{Si}$	140	pPv	$Mg_{8256}Si_{8128}O_{24576}H_{128}$	0.140	115.9	−5.91
$(Mg + 2H)_{Si}$	140	pPv	$Mg_{1088}Si_{960}O_{3072}H_{128}$	1.12	101.6	−6.20

Note. The water content (C_{water}) is obtained by dividing the mass of available H$_2$O by the total mass of all atoms. There are three runs of temperatures of 2000, 3000, and 4000 K for each pressure unless the system is molten or no effective ion hop is observed. All diffusion coefficients as well as uncertainties of ΔH and D_0 are provided in Table S1.

correlation between system size and diffusivity is reminiscent of the liquid phase, for which long-range hydro-dynamic interactions result in a linear decay with the reciprocal spatial scale of the simulation system characterized by the Oseen tensors (Yeh & Hummer, 2004). The associated standard deviation (SD) drops significantly as the system expands (Figure S2 in Supporting Information S1). We characterize uncertainties following the approach proposed by He et al. (2018),

$$\mathrm{SD} = \bar{D} \times \left(\frac{A}{\sqrt{N_{\mathrm{eff}}}} + B \right) \qquad (5)$$

where $\bar{D}$ and SD are the average value and standard deviation of diffusion coefficients, respectively; N_{eff} denotes the total number of effective ion hops; A and B are constants. A larger supercell with a given water content contains more hydrogen atoms, leading to a larger number of effective hydrogen hops, and consequently reducing uncertainties of diffusivity as shown in Figure S2 in Supporting Information S1. The diffusion coefficients reported in Table 1, Table S1, and Table S2 are based on systems consisting of at least 4,000 atoms to guarantee size convergence.

To examine how long of a simulation is sufficient to calculate an adequately accurate diffusion coefficient, we run a long simulation for 10 ns of hydrous bridgmanite ($Mg_{960}Si_{1024}O_{3072}H_{128}$) at 2,000 K and 25 GPa. We take the first 1, 2, 3, 4, 5, and 7 ns segment from this 10 ns trajectory, and then calculate the respective hydrogen diffusion coefficients (Figure S3 in Supporting Information S1). The data point at 1 ns is the average result of 10 independent simulations, while the other data points are obtained from single simulations. The results show that as the simulation time increases, the calculated hydrogen diffusion coefficient gradually converges to the results of the 10 ns simulation. However, even with as short as 1-ns simulation, the maximum deviation is within 20%, and the average value is nearly identical to the 10-ns simulation result. Therefore, we confirm that a 1-ns trajectory is sufficient to obtain an accurate result of the hydrogen diffusion coefficients.

The uncertainties of the calculated diffusivities are evaluated by performing 10 independent simulations with different initial velocity distributions or different defect distributions in the supercell (see Supporting Information). The error bars calculated by the above method are represented by solid lines in the figures. However, due to the limitations of computational resources, it is computationally impractical to perform 10 independent simulations for all data reported in this paper. Therefore, based on our existing results, we estimated the uncertainties of the hydrogen diffusion coefficients for similar systems. The estimated error bars are represented by dashed lines in the figures.

3.3. Hydrogen Diffusion Coefficients in Bridgmanite and Post-Perovskite

Figure S1a in Supporting Information S1 illustrates an example of MSD results for hydrous bridgmanite ($Mg_{15}Si_{16}O_{48}H_2$) at 3,000 K and 25 GPa. During the initial few tens of femtoseconds, MSD as a function of time resembles that of ballistic motion, which means that the motion of particles is predominantly governed by their initial velocities, rather than by interactions with their surroundings or thermal fluctuations. For the calculation of diffusion coefficients, we exclude this ballistic stage and only consider the portion of MSD which is a linear function of time.

We obtain hydrogen diffusion coefficients for both bridgmanite and post-perovskite with four representative water concentrations (∼175 ppm, ∼700 ppm, ∼1,400 ppm, and ∼1.13 wt%), three hydrogen incorporation mechanisms (i.e., $(2H)_{Mg}$, $(4H)_{Si}$, and $(Mg + 2H)_{Si}$), and various pressures and temperatures (Table 1, Table S1, and Table S2).

As an example, Figure 2 summarizes the results for systems that contain 1,400 ppm of water. Similar trends are observed for other water concentrations. Calculations for post-perovskite are conducted only at 140 GPa (Murakami et al., 2004). Bridgmanite melts at 4,000 K and 25 GPa, and thus no data is displayed under this P/T condition. At 2,000 K and 140 GPa, The slopes of all MSD-time plots are close to zero because no effective ion hop is observed during the total simulation time of 1 ns, and thus corresponding diffusivities cannot be derived.
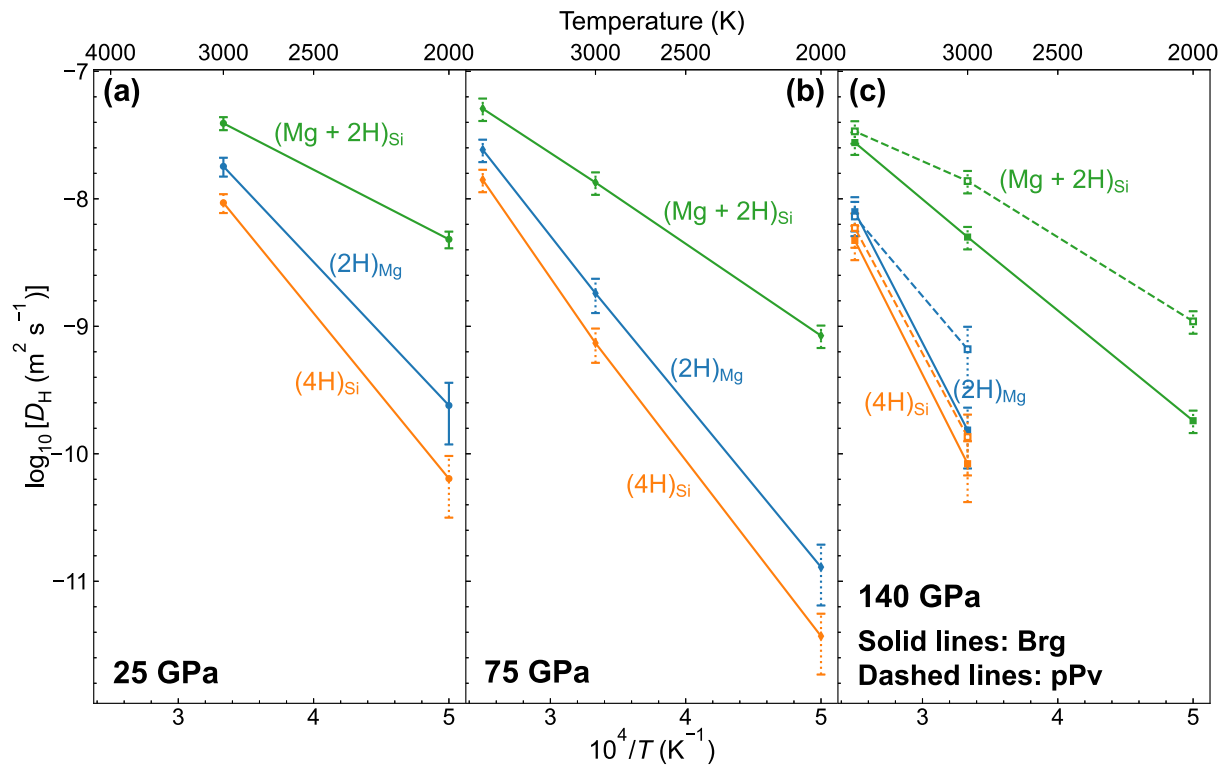
4. Discussion

4.1. Factors Affecting Hydrogen Diffusivity in Bridgmanite and Post-Perovskite

4.1.1. Temperature and Pressure

Hydrogen diffusivity exhibits a significant increase with temperature, following an Arrhenius-type behavior, while it decreases with compression (Figure 2). Table 1 presents pre-exponential factors and activation enthalpies for various defects, pressures, mineral phases, and water contents, calculated based on our hydrogen diffusivity results by fitting into Equation 3. The opposing effects of pressure and temperature along the geotherm (Katsura et al., 2010) lead to a near-constant hydrogen diffusivity throughout most of the lower mantle (see Table S2).

4.1.2. Hydrogen Incorporation Mechanisms

Figure 2 reveals that the diffusivity of hydrogen is the highest when incorporated via the $(Mg + 2H)_{Si}$ defect. Additionally, the $(Al + H)_{Si}$ defect exhibits a hydrogen diffusivity close to $(Mg + 2H)_{Si}$, far surpassing that of the other two defect mechanisms (Figure S8 in Supporting Information S1). To explore the underlying reason, we examine the color mapping trajectories of hydrogen diffusion in hydrous bridgmanite systems with $(2H)_{Mg}$, $(Mg + 2H)_{Si}$, and $(Al + H)_{Si}$ defects (Figure 3 and Figure S7 in Supporting Information S1). We also plot the atomic
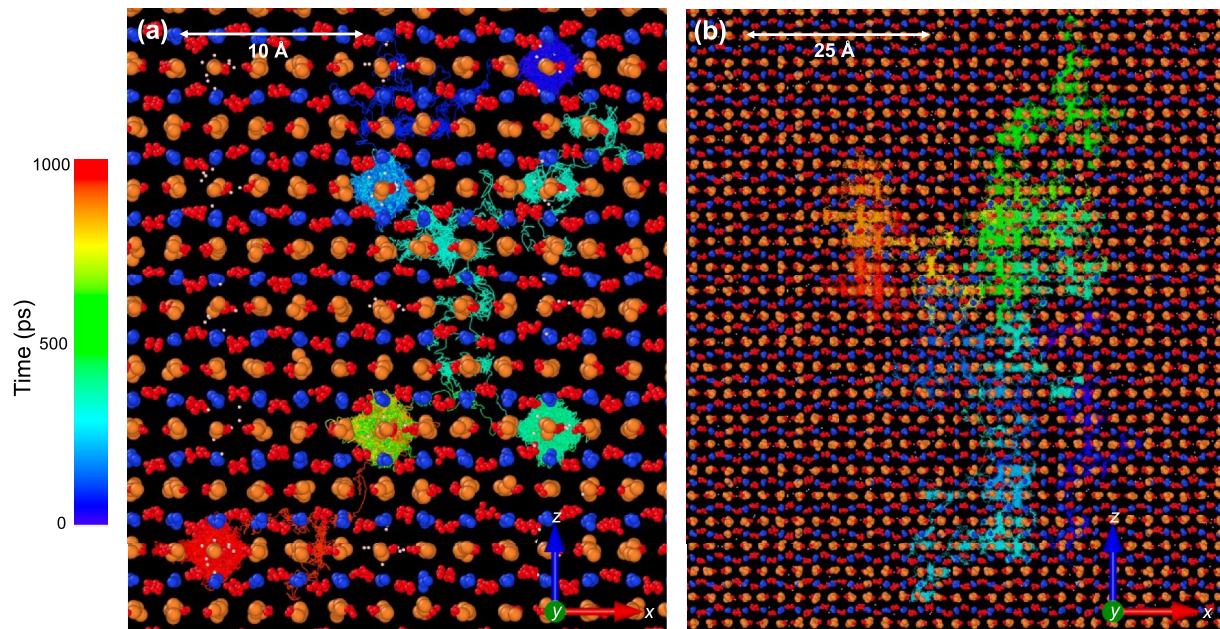
Figure 2. Hydrogen diffusion coefficients in hydrous bridgmanite (Brg, solid lines) and post-perovskite (pPv, dashed lines) as a function of reciprocal temperature (2,000, 3,000, and 4,000 K) for different hydrogen incorporation mechanisms at 25 GPa (a), 75 GPa (b), and 140 GPa (c). The water content of all systems is 1,400 ppm. The $(2H)_{Mg}$ defect ($Mg_{8128}Si_{8192}O_{24576}H_{128}$), the $(4H)_{Si}$ defect ($Mg_{8192}Si_{8160}O_{24576}H_{128}$), and the $(Mg + 2H)_{Si}$ defect ($Mg_{8256}Si_{8128}O_{24576}H_{128}$) are shown in blue, orange, and green, respectively. The solid error bars represent the 2SD of 10 independent simulations. The dashed error bars are estimated based on the error bars of systems with similar diffusion coefficients that have undergone repeated simulations.

positions (Figure S5 in Supporting Information S1) along the three crystallographic axes as a function of time corresponding to the trajectories shown in Figure 3. For the $(2H)_{Mg}$ defect (Figure 3a and Figure S5a in Supporting Information S1), the hydrogen atom spends the majority of the time (about 95%) bound within Mg vacancy sites, while the remaining time is spent jumping and migrating through the interstitial sites. Specifically, the hydrogen atom stays in a Mg vacancy site for 72 ps until it starts a diffusion migration toward another Mg vacancy site. After staying for 228 ps, this hydrogen atom begins its next migration and arrives at another vacancy site at 341 ps. This migration crosses multiple interstitial sites, undergoing several consecutive jumps from one interstitial site to another. After staying for 75 ps, the hydrogen atom moves to the next vacancy site through a rapid diffusion jump that takes only 2 ps, and then jumps to the final vacancy 511 ps later. For the $(Mg + 2H)_{Si}$ defect (Figure 3b, Figures S5b and S7b in Supporting Information S1) and the $(Al + H)_{Si}$ defect (Figure S7a in Supporting Information S1), however, the hydrogen atoms quickly jump through the interstitial sites and do not exhibit prolonged stays at defect sites, showing significantly higher mobility. In this case, the hydrogen diffusivity in bridgmanite exhibits a profound similarity to that in the one-dimensional water channels of stishovite-water superstructures (J. Li et al., 2023). Furthermore, the elevated hydrogen diffusivity may lead to an increase in configurational entropy, a reduction in defect formation free energy, and thus an enhanced stability of $(Mg + 2H)_{Si}$ and $(Al + H)_{Si}$ defects in water-bearing bridgmanite (J. Li et al., 2023; Muir & Brodholt, 2018).

Generally, hydrogen atoms predominantly occupy vacancy or interstitial sites between diffusion jumps. Diffusion occurs through rapid jumps between vacancy or interstitial sites (i.e., effective ion hops), with jump lengths reaching up to several angstroms. The microscopic processes of hydrogen diffusion in bridgmanite and post-perovskite resemble those in wadsleyite and ringwoodite (Caracas & Panero, 2017).

In fact, this microscopic mechanism is closely related to the activation enthalpy in the Arrhenius equation Equation 3. The activation enthalpy is the energy difference between the system when hydrogen occupies the most energetically favorable position and when hydrogen passes the saddle point connecting the two energy
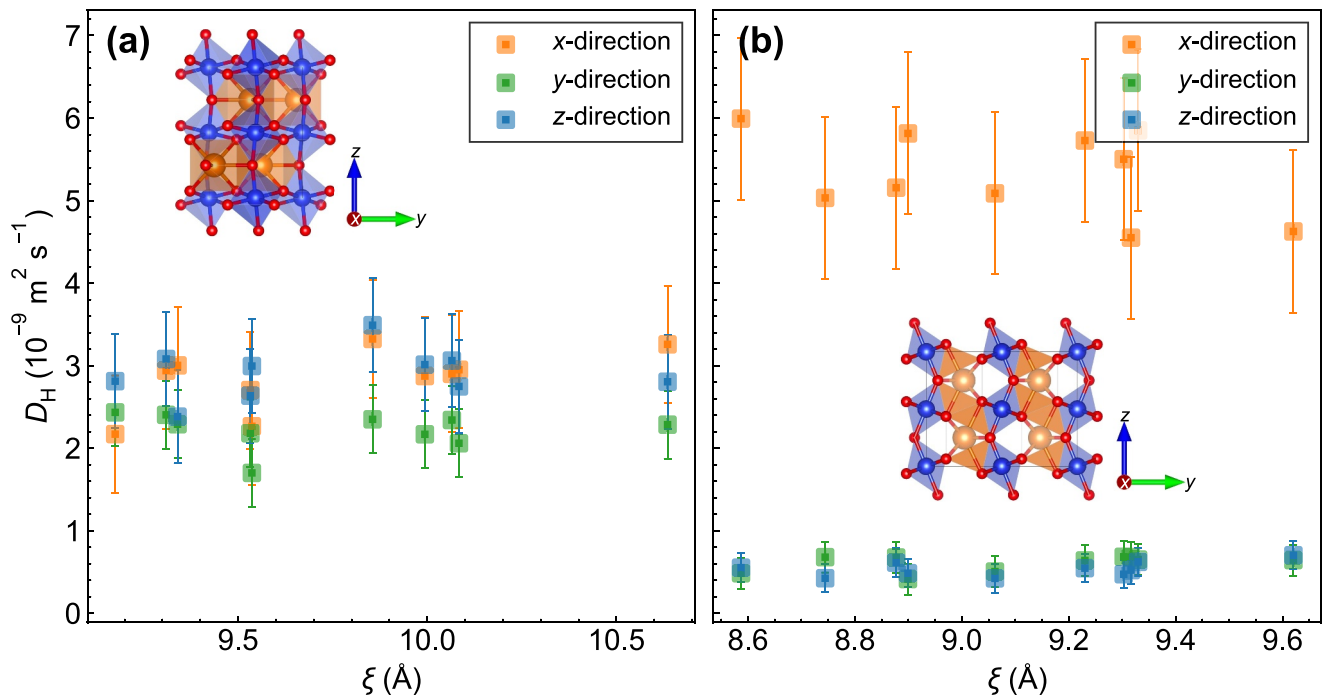
Figure 3. Color mapping of the trajectories of two hydrogen atoms over time in hydrous bridgmanite for (a) the $(2H)_{Mg}$ defect ($Mg_{960}Si_{1024}O_{3072}H_{128}$) and (b) the $(Mg + 2H)_{Si}$ defect ($Mg_{1088}Si_{960}O_{3072}H_{128}$) at 2000 K and 25 GPa. As the simulation time increases from 0 to 1,000 ps, the color of the trajectory changes along the visible spectrum. Orange, blue, red, and white spheres represent magnesium, silicon, oxygen, and hydrogen, respectively. The atomic positions along the three crystallographic axes as a function of time are shown in Figure S5 in Supporting Information S1.

minima (Ingrin & Blanchard, 2006). Activation enthalpies of $(Mg + 2H)_{Si}$ are notably lower than those of $(2H)_{Mg}$ and $(4H)_{Si}$, for both bridgmanite and post-perovskite (Table 1 and Figure S4 in Supporting Information S1). Given that the ionic radius of Mg^{2+} (~86 p.m.) and Al^{3+} (~67.5 p.m.) is larger than that of Si^{4+} (~54 p.m.) (Slater, 1964), Mg and Al can effectively take up most of the space within a Si vacancy, making it difficult for hydrogen atoms to fit in. As such, $(Mg + 2H)_{Si}$ and $(Al + H)_{Si}$ have relatively higher potential energies, and lower activation enthalpies, leading to the fastest hydrogen diffusion across all considered temperatures, pressures, and mineral phases.

4.1.3. Mineral Phases

Bridgmanite and post-perovskite exhibit significantly different characteristics of hydrogen diffusion. Hydrogen diffuses overall faster in post-perovskite than in bridgmanite, particularly at low temperatures (Figure 2c). Furthermore, these two minerals show completely different hydrogen diffusivities along their crystallographic axes (Figure 4). In bridgmanite, for initial configurations with various defect distributions, the error bars of diffusion coefficients along the three directions overlap with each other, exhibiting nearly isotropic hydrogen diffusion. Changes in the defect distribution will affect the order of diffusivity along different directions. In post-perovskite, hydrogen atoms prefer diffusing along [100] (*x*-direction), showing a significant anisotropy. The diffusion coefficient along the [100] direction is nearly an order of magnitude faster than along the [010] and [001] directions. This pattern of anisotropy remains regardless of defect incorporation mechanisms, defect distributions in the supercell, and defect densities considered.

Similar to the anisotropic diffusion of protons in rutile (Farver, 2010) and stishovite-water superstructures (J. Li et al., 2023), the large open channels (see Figure 4b) along the [100] direction in the post-perovskite structure likely provide ample space for hydrogen diffusion pathways, resulting in more efficient hydrogen diffusion along this direction. Different from J. Li et al. (2023), the open channels in post-perovskite are an inherent feature of its crystallography, occurring between the edge-sharing SiO_6 octahedra, rather than being formed due to the incorporation of hydrogen defects. The structural features of post-perovskite result in anisotropic hydrogen diffusion, facilitated by large open channels that enhance diffusivity. Consequently, post-perovskite yields a higher hydrogen diffusivity than bridgmanite, despite its higher density.
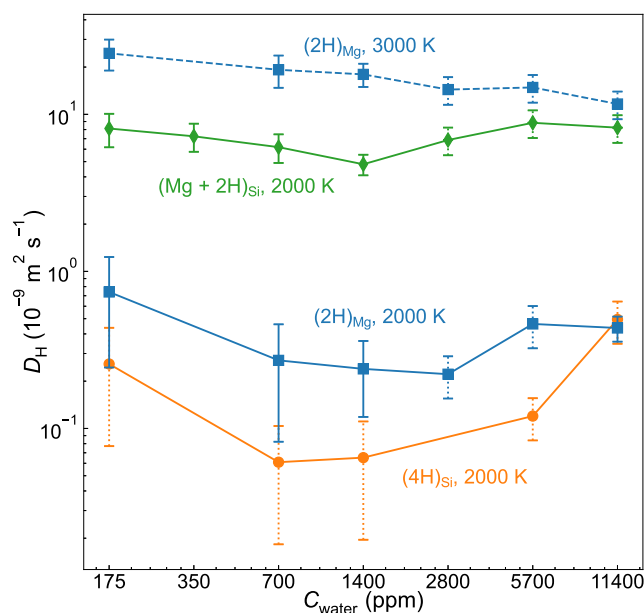
Figure 4. The anisotropy of hydrogen diffusion in hydrous bridgmanite ($Mg_{8128}Si_{8192}O_{24576}H_{128}$) and post-perovskite ($Mg_{8128}Si_{8192}O_{24576}H_{128}$) shown by plotting hydrogen diffusion coefficients along three different crystallographic axes, x (orange), y (green), and z (blue) of 10 random defect distributions as a function of average inter-defect distance of nearest neighbors (ξ), defined in Text S2 in Supporting Information S1. Simulations are performed at 4,000 K and 140 GPa. Orange, blue, and red spheres represent magnesium, silicon, and oxygen, respectively. The error bars represent 2SD of data along each direction.

4.1.4. Water Concentration

Water concentration also affects the hydrogen diffusivity in the host mineral (e.g., Caracas & Panero, 2017). We find that the effects of water content are moderate and nonlinear (Figure 5). At 3,000 K, the hydrogen diffusivity decreases with increasing water content; while at 2,000 K, simulations of all three defect mechanisms show a trend where the diffusivity first increases and then decreases with increasing water content.

To understand the underlying reason for this phenomenon, we compare the microscopic mechanisms of hydrogen diffusion in hydrous bridgmanite systems with the same $(2H)_{Mg}$ defect but different water contents. Figure 3a and Figure S6a in Supporting Information S1 present the hydrogen trajectories of $Mg_{960}Si_{1024}O_{3072}H_{128}$ ($C_{water} = 1.14$ wt%) and $Mg_{16368}Si_{16384}O_{49152}H_{32}$ ($C_{water} = 0.0175$ wt%), respectively. We find that in the simulation with 1.14 wt% water, most (~80%) of hydrogen atoms hop at least twice, passing through multiple vacancy sites, and spend the majority of the simulation time (~95%) residing within these vacancy sites. In contrast, for the simulation with 0.0175 wt% water, only 3 out of the 32 hydrogen atoms successfully migrate to neighboring sites. The other 29 atoms either remain at the initial sites throughout the 1-ns simulation or attempt to migrate but return to their initial positions quickly. Additionally, hydrogen atoms with successful diffusion migration often reside in interstitial sites for a significant amount of time (up to ~500 ps) (Figure S6a in Supporting Information S1).

We believe that water content primarily affects the diffusion coefficient by changing the distance between neighboring vacancy sites. Let us consider two systems with different water contents while the attempt frequency of hydrogen diffusion migration is the same. In the water-rich system, due to the short distance between vacancies, these attempts are more likely to succeed in transporting the hydrogen atom to a new site, achieving net diffusion. This is the reason why we observe more hydrogen atom migrations in Figure 3a than in Figure S6a in Supporting Information S1. In contrast, in the water-poor system, the hydrogen atom struggles to find a stable vacancy site to settle in and frequently returns to the initial defect site under the attraction of a local negative charge. Since the Coulombic force diminishes rapidly with distance ($\propto r^{-2}$), once hydrogen reaches a distance far enough to escape the attraction, it lingers in the interstitial site for a long time and diffuses rapidly (the interstitial

Figure 5. Hydrogen diffusion coefficients in hydrous bridgmanite (chemical compositions are shown in Table 1) as a function of water concentration at 2,000 K (solid lines) and 3,000 K (dashed line). The pressure is 25 GPa. $(2H)_{Mg}$, $(4H)_{Si}$, and $(Mg + 2H)_{Si}$ defects are shown in blue, orange, and green, respectively. The solid error bars represent the 2SD of 10 independent simulations. The dashed error bars are estimated based on the error bars of systems with similar diffusion coefficients that have undergone repeated simulations.

site has high potential energy) until it reaches the next low-energy vacancy site (Figure S6a in Supporting Information S1).

In high-temperature scenarios, the situation is straightforward: since the hydrogen atom is very light, it has high velocity, easily escapes the Coulombic attraction, and diffuses quickly in interstitial sites. An increase in water content (or a decrease in the average distance between vacancies) results in hydrogen being more constrained within the vacancy sites, leading to more pauses during diffusion (Figure 3a). Consequently, the diffusion coefficient decreases monotonically with increasing water content.

In the case of low temperatures, the situation becomes more intricate. The velocity of hydrogen is lower, making it harder to overcome Coulombic attraction and achieve a successful migration attempt. In high water content scenarios (>1,400 ppm), nearby vacancy sites do not act as obstacles to diffusion. Instead, a nearby attractive vacancy can transform a failed migration attempt into a successful one. This is consistent with previous studies on wadsleyite and ringwoodite with high water content, where increasing the defect density may shorten the hopping distance of hydrogen and consequently enhance its diffusion (Caracas & Panero, 2017). However, when the water content decreases to a certain threshold (~1,400 ppm), the nearest defects are too distant to have any significant influence on hydrogen during a migration attempt. The facilitative effect of vacancies disappears, and the only remaining influence is their inhibitory effect on the rapid diffusion in interstitial sites, degenerating to the situation at high temperatures. As a result, the diffusion coefficient of hydrogen first increases and then decreases with increasing water content, reaching a minimum of around 1,400 ppm.
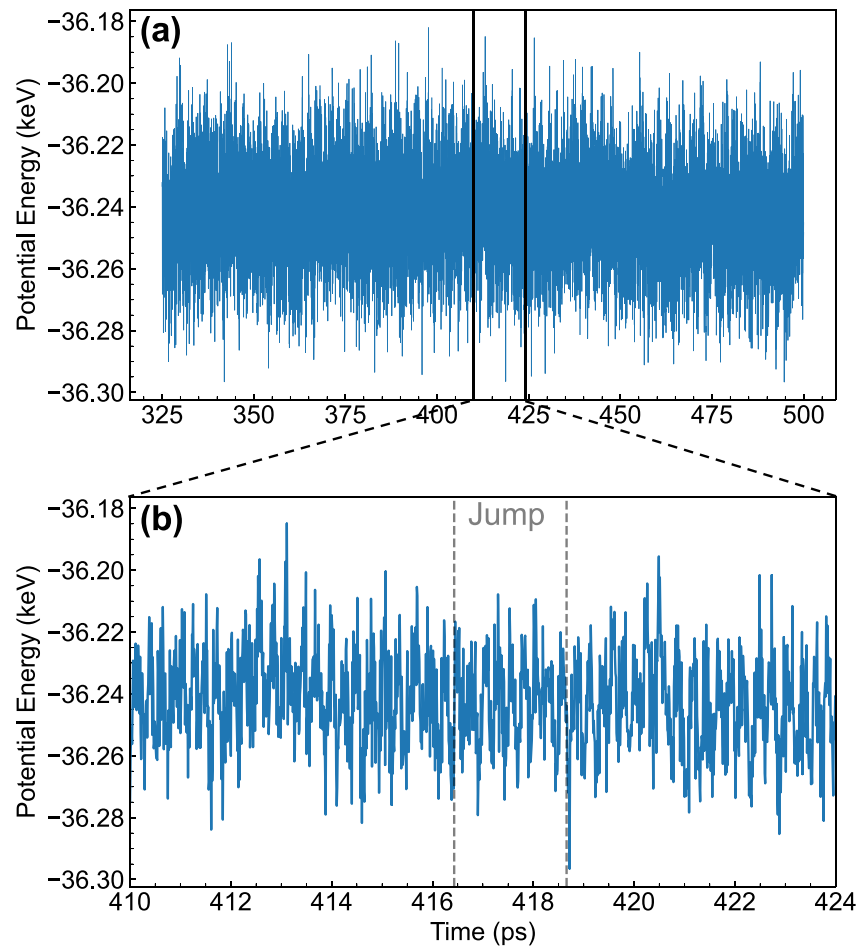
In addition, higher water concentration may cause additional hydrogen to occupy interstitial sites, obstructing some diffusion pathways, and decelerating hydrogen diffusion, similar to the saturation effect in metal-hydrogen systems (e.g., Shelyapina, 2022). With respect to the $(Mg + 2H)_{Si}$ defect, since hydrogen atoms mainly reside in interstitial sites, this can also be a potential factor affecting hydrogen diffusivity.

In summary, hydrogen diffusion as a function of water concentration in mantle minerals is controlled by many competing factors and thus exhibits a complicated dependence on water contents. Nevertheless, for all conditions considered in this study, the variance of diffusion coefficients due to varying water concentrations does not exceed one order of magnitude (Figure 5). Overall, the water content does not have a significant impact on the hydrogen diffusion coefficient. Based on this finding, we conclude that our hydrogen diffusivity results are applicable to the lower mantle given the similar plausible range of water content (Ohtani, 2021).

4.2. Energy Fluctuation

We also monitor potential energy fluctuations upon hydrogen diffusion. The total potential energy of the system does not exhibit a clear local energy maximum or a saddle point during the diffusion jumps of hydrogen (Figure 6) described in Section 4.1.2, Figure 3, and Figure S5 in Supporting Information S1, in contrast to the classical transition state theory (Henkelman et al., 2000). The absence of an energy saddle point may be explained by the low concentration of hydrogen (thousands of ppm) considered in this study, which dilutes the effect of diffusion on the total potential energy of the entire system. Another possibility is that other atoms within the system also adjust their positions when diffusion occurs. This behavior highlights the intricate interplay between the positions of all atoms in the lattice and the total energy of the system, rather than just the positions of diffusing atoms. This result is consistent with the energy fluctuation observed during hydrogen diffusion in wadsleyite and ringwoodite (Caracas & Panero, 2017).

Figure 6. Potential energy fluctuations of hydrous bridgmanite ($Mg_{960}Si_{1024}O_{3072}H_{128}$) at 2,000 K and 25 GPa during the MD simulation. The corresponding trajectory is described in Section 4.1.2, Figure 3a, and Figure S5a in Supporting Information S1.
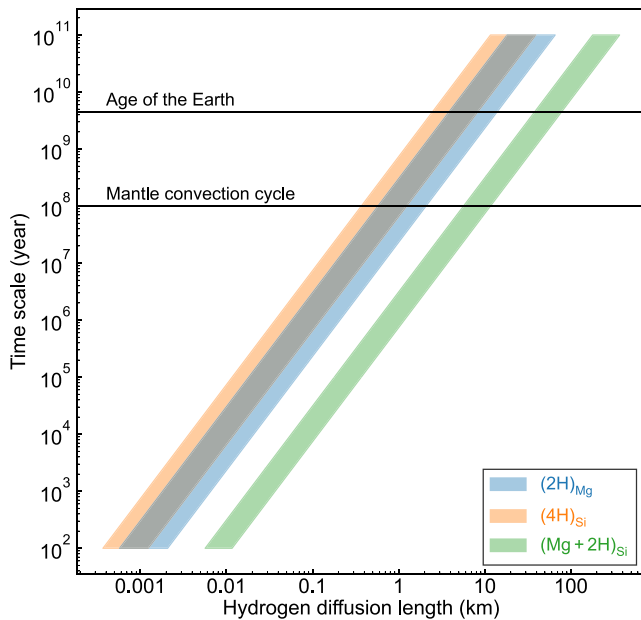
4.3. Self- and Chemical Diffusion of Hydrogen in Mantle Silicates

Self-diffusion is the process where chemically identical atoms move within a homogeneous material, while chemical diffusion involves the movement of atoms from areas of high concentration to low concentration. The values of self-diffusion and chemical diffusion coefficients are generally not the same. The above discussions focus on the self-diffusion of hydrogen since the simulated system does not exhibit a concentration gradient of both hydrogen and defects. As the transport of water in the Earth's interior often occurs with a concentration gradient, the chemical diffusion of hydrogen in mantle silicates becomes crucial.

Different mechanisms have been proposed for the chemical diffusion of hydrogen in mantle silicates. First, protons may diffuse in interstitial sites and the proton flux is coupled with a counter flux of polarons, facilitated by the mobile excess charge on ferric iron ($Fe^{2+} \rightleftharpoons Fe^{3+} + e^-$) (e.g., Hae et al., 2006; Kohlstedt & Mackwell, 1998; Mackwell & Kohlstedt, 1990). Here, polarons are quasiparticles formed by an excess charge carrier (electron or hole) localized within a potential well, self-generated by displacing the surrounding ions (Franchini et al., 2021). Since the diffusivity of polarons significantly surpasses that of protons (Schmalzried & Schmalzried, 1974), the chemical diffusivity $\widetilde{D}_H$ can be written as (Hae et al., 2006; Kohlstedt & Mackwell, 1998),

$$\widetilde{D}_H = \frac{2D_P D_H}{D_P + D_H} \approx 2D_H \tag{6}$$

Figure 7. Hydrogen diffusion time scales (t) as a function of hydrogen diffusion length scales $\left(L_d = \sqrt{2\widetilde{D}_H t} \right)$. The left and right boundaries of the shaded area correspond to the minimum and maximum values obtained from simulations along the mantle geotherm (Katsura et al., 2010) considering various hydrogen incorporation mechanisms, and water contents (Table S2). The estimated mantle convection cycle (100 Ma, Holzapfel et al., 2005) and the age of the Earth (4.5 Ga) are also shown. $(2H)_{Mg}$, $(4H)_{Si}$, and $(Mg + 2H)_{Si}$ defects are shown in blue, orange, and green, respectively.

where D_H and D_P are the self-diffusion coefficients of hydrogen and polaron, respectively. Thus, the chemical diffusivity of hydrogen can be directly estimated using the self-diffusivity obtained in this study. Second, hydrogen diffusion can be coupled with the diffusion of intrinsic point defects such as Mg and Si vacancies (e.g., Demouchy & Mackwell, 2003; Kohlstedt & Mackwell, 1998). In this case, the chemical diffusion of hydrogen is much slower (two orders of magnitude slower than the first mechanism (Kohlstedt & Mackwell, 1998)), and the self-diffusivity of hydrogen may not effectively constrain its chemical diffusivity. Third, activated hydrogen atoms may dissociate from a thermal vacancy and migrate as an interstitial particle until it is trapped again at another thermal vacancy, known as the dissociative mechanism (Frank & Turnbull, 1956; Novella et al., 2017). This closely resembles the self-diffusion of hydrogen in our simulations (see Section 4.1.2 and Section 4.1.4). This dissociative mechanism can well explain why the self-/chemical diffusivity of hydrogen (e.g., Hae et al., 2006; Novella et al., 2017) is close to the diffusivity of small polarons (Novella et al., 2017), but much higher than those of Mg and Si in mantle silicates (e.g., J. Xu et al., 2011).

Furthermore, we note that Al might be extensively present in the lower mantle (e.g., Irifune, 1994) and thus calculate the diffusion coefficient of hydrogen in Al-bearing bridgmanite at 2,000 K and 25 GPa (Text S3 in Supporting Information S1). Intriguingly, this diffusion is independent of any vacancy movement, as the incorporation of hydrogen does not rely on the presence of such vacancies. Given that Al^{3+} bears one less positive charge than Si^{4+}, and the bridgmanite crystal remains electrically neutral, the non-protonated Al^{3+} ions might be associated with Fe^{3+} (McCammon, 1997). This suggests that the chemical diffusion of hydrogen in Al-bearing bridgmanite could also potentially involve the flux of excess charge on ferric iron, showing a similar pattern with the self-diffusion.

4.4. The Water Distribution in the Lower Mantle

Hydrous minerals in the subducted oceanic crust may transport a substantial amount of water into the Earth's deep interior, reaching as deep down as the core-mantle boundary (e.g., Ohtani, 2015). In addition, the low D/H ratio in Baffin Island and Icelandic lavas suggests the existence of primordial hydrogen reservoirs in the lower mantle that inherited the D/H ratio directly from the protosolar nebula (Hallis et al., 2015). Furthermore, previous experimental and observational studies suggest a heterogeneous water distribution in the mantle transition zone (Hae et al., 2006; Sun et al., 2015; Zhou et al., 2022).

Bridgmanite is the most abundant mineral phase of the lower mantle. Hernández et al. (2013) found that the partition coefficient of water between ferropericlase and bridgmanite is around 90 at 24 GPa using ab initio methods. This suggests that the water content in bridgmanite is about two orders of magnitude higher than in coexisting ferropericlase, the second most abundant lower mantle mineral, aligning with average estimates of water solubility in them (Lu & Li, 2023). Furthermore, Muir and Brodholt (2018) calculated water distribution among various lower mantle mineral phases, revealing that for a few hundred ppm of water in the lower mantle, most of the water is partitioned into Al-bearing bridgmanite. Therefore, the main medium for water transport in the lower mantle may be bridgmanite. To evaluate the effect of hydrogen diffusivity on the distribution of water in the lower mantle, we calculate hydrogen diffusion length scales for bridgmanite and post-perovskite, based on hydrogen diffusion coefficients derived along the mantle geotherm (Katsura et al., 2010) (Figure 7). The diffusion length scale is given by $L_d = \sqrt{2\widetilde{D}_H t}$, where $\widetilde{D}_H$ is the estimated chemical diffusivity of hydrogen (Equation 6) and t represents the time scale, considering the first chemical diffusion mechanism as discussed in Section 4.3. With an assumed mantle convection velocity of 5 cm per year, the estimated time scale for one mantle convection cycle is ~100 Ma (Holzapfel et al., 2005). The corresponding hydrogen diffusion length scales in bridgmanite and post-perovskite are less than 12 km, regardless of depths, water content, and hydrogen incorporation mechanisms

(assuming $(Mg + 2H)_{Si}$ and $(Al + H)_{Si}$ are analogs regarding hydrogen diffusion). Considering that a portion of water may undergo much slower chemical diffusion coupled with cation vacancies (Section 4.3), this diffusion length would be even shorter. Therefore, water brought into the lower mantle by the subducting slabs would be locally confined, leading to a heterogeneous distribution of water throughout the Earth's lower mantle. However, other important factors that might influence hydrogen diffusion behavior in bridgmanite, such as grain boundary diffusion and compositional effects (e.g., iron content), need further study to corroborate this conclusion.
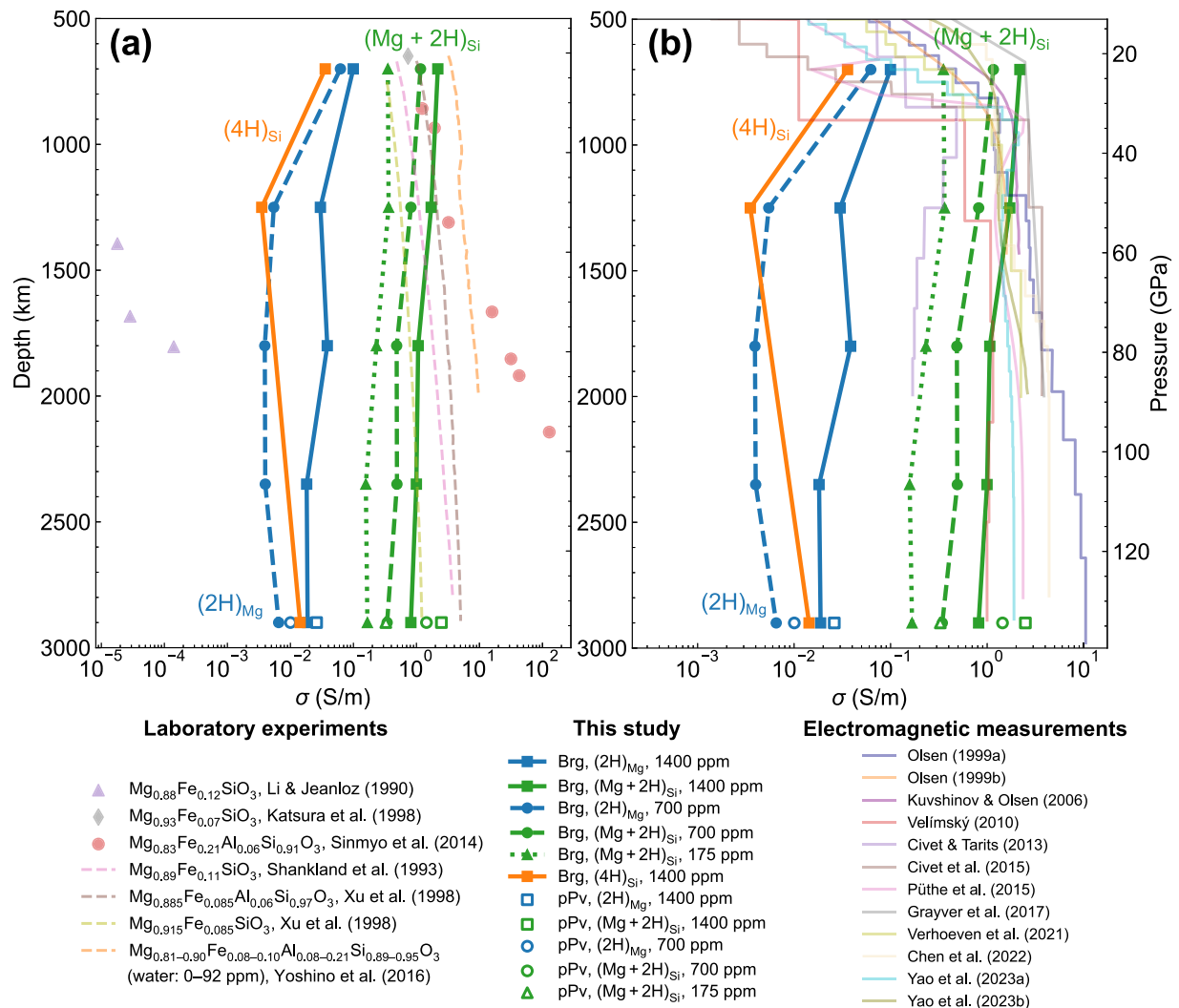
4.5. The Electrical Conductivity in the Lower Mantle

The electrical conductivity of mantle silicates is mainly contributed by four conduction mechanisms: ionic conduction, hopping (small polaron) conduction, large polaron conduction, and proton conduction (Yoshino, 2010). Due to its low bonding energy and small ionic radius, the energy barrier of the transiting proton is relatively low, causing proton conductivity to potentially dominate the bulk conductivity under wet conditions (Sun et al., 2015; Yoshino, 2010).

In this study, we employ the Nernst-Einstein equation (Equation 4) to calculate the proton conductivity in bridgmanite and post-perovskite, based on hydrogen diffusivities obtained from MD simulations along the geotherm (Katsura et al., 2010) (Table S2). Proton conductivity results for various systems are plotted as a function of depth, along with experimental results (Figure 8a) and observations (Figure 8b) of the bulk conductivity of the lower mantle. The proton conductivity of bridgmanite is sensitive to the water content and hydrogen incorporation mechanisms. If water content remains constant and the hydrogen incorporation mechanism is consistent throughout the lower mantle, the proton conductivity would show relatively low depth sensitivity due to the near-constant hydrogen diffusivity. The diffusivity of hydrogen is the largest when incorporated as $(Mg + 2H)_{Si}$ defects (or the diffusionally analogous $(Al + H)_{Si}$ defects), resulting in the highest proton conductivity of up to 1 S m^{-1} (Table S2 and Figure 8). Under the lowermost mantle conditions, the proton conductivity in post-perovskite is higher than that in bridgmanite, with the difference within one order of magnitude.

Figure 8a presents experimentally measured conductivity results of dry bridgmanite with various Fe and Al contents (Katsura et al., 1998; X. Y. Li & Jeanloz, 1990; Shankland et al., 1993; Sinmyo et al., 2014; Y. S. Xu et al., 1998), except for one study that used bridgmanite samples containing 0–92 ppm water (Yoshino et al., 2016). These experimental results, although highly scattered, suggest that the conductivity of bridgmanite is sensitive to chemical compositions, for example, Al and Fe contents. The relatively high conductivity results measured by Yoshino et al. (2016), compared to other studies, may be caused by the presence of water in their samples. We find that the contribution of proton for Earth-relevant water contents is comparable to the sum of all other three conduction mechanisms in bridgmanite (i.e., the conductivity of dry bridgmanite) when hydrogen is incorporated as $(Mg + 2H)_{Si}$ or $(Al + H)_{Si}$ defects. The 1D conductivity-depth profiles in the lower mantle, as determined from electromagnetic induction studies, are shown in Figure 8b (Chen et al., 2022; Civet et al., 2015; Civet & Tarits, 2013; Grayver et al., 2017; Kuvshinov & Olsen, 2006; Olsen, 1999a, 1999b; Puthe et al., 2015; Velimsky, 2010; Verhoeven et al., 2021; Yao, Ren, Pan, et al., 2023; Yao, Ren, Tang, et al., 2023). Most of these conductivity data fall within two orders of magnitude (0.1–10 S m^{-1}) and generally remain nearly constant or slightly increase with increasing depth. Considering $(Mg + 2H)_{Si}$ or $(Al + H)_{Si}$ defects, our results of proton conductivity are within the same magnitude as the measured conductivity, supporting the potential role of water in affecting the electrical conductivity of the lower mantle.

Previous studies reported strong lateral heterogeneities of the electrical conductivity in the mid-lower mantle regions (e.g., Khan et al., 2011; Tarits & Mandea, 2010). Since the proton conductivity in bridgmanite is sensitive to both temperature and water content, the possible thermal anomalies (Hsieh et al., 2020) as well as the potential heterogeneous water distribution discussed in Section 4.4 may lead to these heterogeneities of the lower mantle conductivity. If we consider bridgmanite with relatively high but still reasonable water contents, for example, around 700 ppm (assuming it primarily exists in the form of $(Mg + 2H)_{Si}$ or $(Al + H)_{Si}$), the proton conductivity is ~1 S m^{-1} at 900 km depth, which aligns perfectly with the heterogeneity in the observed mantle conductivity at a depth of 900 km (1.4–2.4 S m^{-1}, Khan et al., 2011). Therefore, water may act as a significant charge carrier in the hydrated regions of the lower mantle, and contribute to the heterogeneity of electrical conductivity. Further, by analyzing electrical conductivity variations, we can potentially deduce water distribution in the lower mantle. It is worth noting that the strong anisotropic hydrogen diffusion in post-perovskite discussed in Section 4.1.3 may

Figure 8. Proton conductivities of bridgmanite (solid symbols) and post-perovskite (empty symbols) compared to experimentally measured electrical conductivities of bridgmanite (a) and bulk conductivities of the lower mantle measured with electromagnetic induction (b). All simulations are performed along an adiabatic geotherm (Katsura et al., 2010), considering various water contents and hydrogen incorporation mechanisms (1,400 ppm: solid thick lines; 700 ppm: dashed thick lines; 175 ppm: dotted thick lines; $(2H)_{Mg}$: blue; $(4H)_{Si}$: orange; $(Mg + 2H)_{Si}$: green). Some data points for $(4H)_{Si}$ defects are not shown since no effective ion hop is observed during the entire simulation time of up to ∼ns. Semi-transparent data points denote the experimentally measured conductivity of dry bridgmanite. Semi-transparent dashed lines represent the lower mantle conductivity models based on experimental results. Semi-transparent solid lines show the 1D electrical conductivity profile determined from electromagnetic induction studies.

result in anisotropic electrical conductivity, similar to the case with olivine in the upper mantle (Bahr & Simpson, 2002).

We acknowledge that real-world scenarios involve a multitude of factors influencing hydrogen diffusivity and electrical conductivity. However, considering this is the first study on the diffusion of hydrogen in lower mantle minerals, we position our results as an initial step and believe our current results provide a foundational step toward creating more comprehensive models that can capture the multifaceted nature of diffusion processes in the Earth's mantle.

5. Conclusions

We have developed a unified MLP of ab initio quality, which, for the first time, enables a comprehensive examination of hydrogen diffusion in bridgmanite and post-perovskite under the Earth's lower mantle conditions.

Our systematic analysis of factors influencing hydrogen diffusivity demonstrates that hydrogen diffusion is highly sensitive to defect mechanism, temperature, and pressure, while relatively insensitive to water content. The trade-off between pressure and temperature leads to a nearly constant hydrogen diffusivity in the lower mantle along the geotherm. Among the four defect mechanisms examined, $(Mg + 2H)_{Si}$ and $(Al + H)_{Si}$ show similar patterns and yield the highest hydrogen diffusivity, which may result from the low activation enthalpy. Hydrogen diffuses overall faster in post-perovskite than in bridgmanite, especially at relatively low temperatures. In addition, these two minerals exhibit distinct anisotropies of hydrogen diffusion. Based on our diffusivity results, we conclude that hydrogen diffusion is sluggish on the geological time scale, suggesting that the water distribution in the lower mantle may be localized and highly heterogeneous. We also calculate the electrical conductivities contributed by hydrogen diffusion in bridgmanite and post-perovskite. When hydrogen incorporates via $(Mg + 2H)_{Si}$ and $(Al + H)_{Si}$ defects, the proton conductivity of bridgmanite falls within the same order of magnitude as the reported lower mantle conductivity profile and can well explain its lateral heterogeneity, indicating that one can potentially deduce water distribution by analyzing electrical conductivity variations in the lower mantle.

Data Availability Statement

All the data and source codes used in this study are stored at the Open Science Framework (https://osf.io/brwcv/) via DOI 10.17605/OSF.IO/BRWCV (Peng & Deng, 2023). Part of our training set and test set for the MLP can be also found in Deng et al. (2023b). For the software packages used in this study, VASP is a commercial code available at https://www.vasp.at; DeePMD-kit is developed openly at https://github.com/deepmodeling/deepmd-kit; LAMMPS is developed openly at https://github.com/lammps/lammps and available at Plimpton et al. (2021); PLUMED 2 is developed openly at https://github.com/plumed/plumed2; ASAP is developed openly at https://github.com/BingqingCheng/ASAP.

References

Bahr, K., & Simpson, F. (2002). Electrical anisotropy below slow- and fast-moving plates: Paleoflow in the upper mantle? *Science*, *295*(5558), 1270–1272. https://doi.org/10.1126/science.1066161

Caracas, R., & Panero, W. R. (2017). Hydrogen mobility in transition zone silicates. *Progress in Earth and Planetary Science*, *4*(1), 11. https://doi.org/10.1186/s40645-017-0119-8

Chen, C., Kuvshinov, A., Kruglyakov, M., Munch, F., & Rigaud, R. (2022). Constraining the crustal and mantle conductivity structures beneath islands by a joint inversion of multi-source magnetic transfer functions. *Journal of Geophysical Research: Solid Earth*, *128*(1), e2022JB024106. https://doi.org/10.1029/2022jb024106

Cheng, B. Q., Griffiths, R. R., Wengert, S., Kunkel, C., Stenczel, T., Zhu, B. N., et al. (2020). Mapping materials and molecules. *Accounts of Chemical Research*, *53*(9), 1981–1991. https://doi.org/10.1021/acs.accounts.0c00403

Civet, F., & Tarits, P. (2013). Analysis of magnetic satellite data to infer the mantle electrical conductivity of telluric planets in the solar system. *Planetary and Space Science*, *84*, 102–111. https://doi.org/10.1016/j.pss.2013.05.004

Civet, F., Thebault, E., Verhoeven, O., Langlais, B., & Saturnino, D. (2015). Electrical conductivity of the Earth's mantle from the first Swarm magnetic field measurements. *Geophysical Research Letters*, *42*(9), 3338–3346. https://doi.org/10.1002/2015gl063397

Demouchy, S., & Mackwell, S. (2003). Water diffusion in synthetic iron-free forsterite. *Physics and Chemistry of Minerals*, *30*(8), 486–494. https://doi.org/10.1007/s00269-003-0342-2

Deng, J., Niu, H., Hu, J., Chen, M., & Stixrude, L. (2023a). Melting of $MgSiO_3$ determined by machine learning potentials. *Physical Review B*, *107*(6), 064103. https://doi.org/10.1103/PhysRevB.107.064103

Deng, J., Niu, H., Hu, J., Chen, M., & Stixrude, L. (2023b). Train and test data [Dataset]. *OSF*. https://doi.org/10.17605/OSF.IO/DT4XS

Deng, J., & Stixrude, L. (2021a). Deep fractionation of Hf in a solidifying magma ocean and its implications for tungsten isotopic heterogeneities in the mantle. *Earth and Planetary Science Letters*, *562*, 8. https://doi.org/10.1016/j.epsl.2021.116873

Deng, J., & Stixrude, L. (2021b). Thermal conductivity of silicate liquid determined by machine learning potentials. *Geophysical Research Letters*, *48*(17), 10. https://doi.org/10.1029/2021gl093806

Farver, J. R. (2010). Oxygen and hydrogen diffusion in minerals. *Reviews in Mineralogy and Geochemistry*, *72*(1), 447–507. https://doi.org/10.2138/rmg.2010.72.10

Fiquet, G., Auzende, A. L., Siebert, J., Corgne, A., Bureau, H., Ozawa, H., & Garbarino, G. (2010). Melting of Peridotite to 140 Gigapascals. *Science*, *329*(5998), 1516–1518. https://doi.org/10.1126/science.1192448

Franchini, C., Reticcioli, M., Setvin, M., & Diebold, U. (2021). Polarons in materials. *Nature Reviews Materials*, *6*(7), 560–586. https://doi.org/10.1038/s41578-021-00289-w

Frank, F. C., & Turnbull, D. (1956). Mechanism of diffusion of Copper in Germanium. *Physical Review*, *104*(3), 617–618. https://doi.org/10.1103/PhysRev.104.617

Freitas, R., & Cao, Y. (2022). Machine-learning potentials for crystal defects. *MRS Communications*, *12*(5), 510–520. https://doi.org/10.1557/s43579-022-00221-5

Fu, S. Y., Yang, J., Karato, S., Vasiliev, A., Presniakov, M. Y., Gavriliuk, A. G., et al. (2019). Water concentration in single-crystal (Al,Fe)-bearing bridgmanite grown from the hydrous melt: Implications for dehydration melting at the topmost lower mantle. *Geophysical Research Letters*, *46*(17–18), 10346–10357. https://doi.org/10.1029/2019gl084630

Grayver, A. V., Munch, F. D., Kuvshinov, A. V., Khan, A., Sabaka, T. J., & Toffner-Clausen, L. (2017). Joint inversion of satellite-detected tidal and magnetospheric signals constrains electrical conductivity and water content of the upper mantle and transition zone. *Geophysical Research Letters*, *44*(12), 6074–6081. https://doi.org/10.1002/2017gl073446

Hae, R., Ohtani, E., Kubo, T., Koyama, T., & Utada, H. (2006). Hydrogen diffusivity in wadsleyite and water distribution in the mantle transition zone. *Earth and Planetary Science Letters*, *243*(1–2), 141–148. https://doi.org/10.1016/j.epsl.2005.12.035

Hallis, L. J., Huss, G. R., Nagashima, K., Taylor, G. J., Halldorsson, S. A., Hilion, D. R., et al. (2015). Evidence for primordial water in Earth's deep mantle. *Science*, *350*(6262), 795–797. https://doi.org/10.1126/science.aac4834

He, X. F., Zhu, Y. Z., Epstein, A., & Mo, Y. F. (2018). Statistical variances of diffusional properties from ab initio molecular dynamics simulations. *Npj Computational Materials*, *4*(1), 9. https://doi.org/10.1038/s41524-018-0074-y

Henkelman, G., Uberuaga, B. P., & Jonsson, H. (2000). A climbing image nudged elastic band method for finding saddle points and minimum energy paths. *Journal of Chemical Physics*, *113*(22), 9901–9904. https://doi.org/10.1063/1.1329672

Hernández, E. R., Alfè, D., & Brodholt, J. (2013). The incorporation of water into lower-mantle perovskites: A first-principles study. *Earth and Planetary Science Letters*, *364*, 37–43. https://doi.org/10.1016/j.epsl.2013.01.005

Holzapfel, C., Rubie, D. C., Frost, D. J., & Langenhorst, F. (2005). Fe-Mg interdiffusion in $(Mg,Fe)SiO_3$ perovskite and lower mantle reequilibration. *Science*, *309*(5741), 1707–1710. https://doi.org/10.1126/science.1111895

Hoover, W. G. (1985). Canonical dynamics - Equilibrium phase-space distributions. *Physical Review A*, *31*(3), 1695–1697. https://doi.org/10.1103/PhysRevA.31.1695

Hsieh, W. P., Ishii, T., Chao, K. H., Tsuchiya, J., Deschamps, F., & Ohtani, E. (2020). Spin transition of iron in delta-(Al,Fe)OOH induces thermal anomalies in earth's lower mantle. *Geophysical Research Letters*, *47*(4), 10. https://doi.org/10.1029/2020gl087036

Imbalzano, G., Anelli, A., Giofre, D., Klees, S., Behler, J., & Ceriotti, M. (2018). Automatic selection of atomic fingerprints and reference configurations for machine-learning potentials. *Journal of Chemical Physics*, *148*(24), 9. https://doi.org/10.1063/1.5024611

Ingrin, J., & Blanchard, M. (2006). Diffusion of hydrogen in minerals. *Reviews in Mineralogy and Geochemistry*, *62*(1), 291–320. https://doi.org/10.2138/rmg.2006.62.13

Irifune, T. (1994). Absence of an aluminous phase in the upper part of the Earth's lower mantle. *Nature*, *370*(6485), 131–133. https://doi.org/10.1038/370131a0

Ishii, T., Ohtani, E., & Shatskiy, A. (2022). Aluminum and hydrogen partitioning between bridgmanite and high-pressure hydrous phases: Implications for water storage in the lower mantle. *Earth and Planetary Science Letters*, *583*, 117441. https://doi.org/10.1016/j.epsl.2022.117441

Karato, S. (1990). The role of hydrogen in the electrical-conductivity of the upper mantle. *Nature*, *347*(6290), 272–273. https://doi.org/10.1038/347272a0

Karato, S. (1995). Effects of water on seismic-wave velocities in the upper-mantle. *Proceedings of the Japan Academy - Series B: Physical & Biological Sciences*, *71*(2), 61–66. https://doi.org/10.2183/pjab.71.61

Karato, S., Paterson, M. S., & Fitz Gerald, J. D. (1986). Rheology of synthetic olivine aggregates - Influence of grain-size and water. *Journal of Geophysical Research-Solid Earth and Planets*, *91*(B8), 8151–8176. https://doi.org/10.1029/JB091iB08p08151

Karki, B. B. (2015). First-principles computation of mantle materials in crystalline and amorphous phases. *Physics of the Earth and Planetary Interiors*, *240*, 43–69. https://doi.org/10.1016/j.pepi.2014.11.004

Katsura, T., Sato, K., & Ito, E. (1998). Electrical conductivity of silicate perovskite at lower-mantle conditions. *Nature*, *395*(6701), 493–495. https://doi.org/10.1038/26736

Katsura, T., Yoneda, A., Yamazaki, D., Yoshino, T., & Ito, E. (2010). Adiabatic temperature profile in the mantle. *Physics of the Earth and Planetary Interiors*, *183*(1–2), 212–218. https://doi.org/10.1016/j.pepi.2010.07.001

Khan, A., Kuvshinov, A., & Semenov, A. (2011). On the heterogeneous electrical conductivity structure of the Earth's mantle with implications for transition zone water content. *Journal of Geophysical Research*, *116*(B1), B01103. https://doi.org/10.1029/2010JB007458

Kohlstedt, D. L., & Mackwell, S. J. (1998). Diffusion of hydrogen and intrinsic point defects in olivine. *Zeitschrift fur Physikalische Chemie*, *207*(1–2), 147–162. https://doi.org/10.1524/zpch.1998.207.part_1_2.147

Kresse, G., & Furthmuller, J. (1996). Efficient iterative schemes for ab initio total-energy calculations using a plane-wave basis set. *Physical Review B*, *54*(16), 11169–11186. https://doi.org/10.1103/PhysRevB.54.11169

Kresse, G., & Joubert, D. (1999). From ultrasoft pseudopotentials to the projector augmented-wave method. *Physical Review B*, *59*(3), 1758–1775. https://doi.org/10.1103/PhysRevB.59.1758

Kudoh, Y., & Inoue, T. (1999). Mg-vacant structural modules and dilution of the symmetry of hydrous wadsleyite, β-$Mg_{2-x}SiH_{2x}O_4$ with $0.00 \leq x \leq 0.25$. *Physics and Chemistry of Minerals*, *26*(5), 382–388. https://doi.org/10.1007/s002690050198

Kuvshinov, A., & Olsen, N. (2006). A global model of mantle conductivity derived from 5 years of CHAMP, Orsted, and SAC-C magnetic data. *Geophysical Research Letters*, *33*(18), 5. https://doi.org/10.1029/2006gl027083

Li, J., Lin, Y., Meier, T., Liu, Z., Yang, W., Mao, H.-k., et al. (2023). Silica-water superstructure and one-dimensional superionic conduit in Earth's mantle. *Science Advances*, *9*(35), eadh3784. https://doi.org/10.1126/sciadv.adh3784

Li, X. Y., & Jeanloz, R. (1990). Laboratory studies of the electrical-conductivity of silicate perovskites at high-pressures and temperatures. *Journal of Geophysical Research-Solid Earth and Planets*, *95*(B4), 5067–5078. https://doi.org/10.1029/JB095iB04p05067

Liu, Z., Fei, H., Chen, L., McCammon, C., Wang, L., Liu, R., et al. (2021). Bridgmanite is nearly dry at the top of the lower mantle. *Earth and Planetary Science Letters*, *570*, 117088. https://doi.org/10.1016/j.epsl.2021.117088

Lu, W., & Li, Y. (2023). Solubility of water in bridgmanite. *Acta Geochimica*, *42*(6), 998–1006. https://doi.org/10.1007/s11631-023-00642-6

Mackwell, S. J., & Kohlstedt, D. L. (1990). Diffusion of hydrogen in olivine: Implications for water in the mantle. *Journal of Geophysical Research*, *95*(B4), 5079–5088. https://doi.org/10.1029/JB095iB04p05079

McCammon, C. (1997). Perovskite as a possible sink for ferric iron in the lower mantle. *Nature*, *387*(6634), 694–696. https://doi.org/10.1038/42685

Mermin, N. D. (1965). Thermal properties of the inhomogeneous electron gas. *Physical Review*, *137*(5A), 1441–A1443. https://doi.org/10.1103/PhysRev.137.A1441

Muir, J. M. R., & Brodholt, J. P. (2018). Water distribution in the lower mantle: Implications for hydrolytic weakening. *Earth and Planetary Science Letters*, *484*, 363–369. https://doi.org/10.1016/j.epsl.2017.11.051

Murakami, M., Hirose, K., Kawamura, K., Sata, N., & Ohishi, Y. (2004). Post-perovskite phase transition in $MgSiO_3$. *Science (New York, N.Y.)*, *304*(5672), 855–858. https://doi.org/10.1126/science.1095932

Niu, H., Bonati, L., Piaggi, P. M., & Parrinello, M. (2020). Ab initio phase diagram and nucleation of gallium. *Nature Communications*, *11*(2654), 2654. https://doi.org/10.1038/s41467-020-16372-9

Novella, D., Jacobsen, B., Weber, P. K., Tyburczy, J. A., Ryerson, F. J., & Du Frane, W. L. (2017). Hydrogen self-diffusion in single crystal olivine and electrical conductivity of the Earth's mantle. *Scientific Reports*, *7*(1), 5344. https://doi.org/10.1038/s41598-017-05113-6

Ohtani, E. (2015). Hydrous minerals and the storage of water in the deep mantle. *Chemical Geology*, *418*, 6–15. https://doi.org/10.1016/j.chemgeo.2015.05.005

Ohtani, E. (2021). Hydration and dehydration in Earth's interior. In R. Jeanloz & K. H. Freeman (Eds.), *Annual review of earth and planetary sciences* (Vol. 49, pp. 253–278). https://doi.org/10.1146/annurev-earth-080320-062509

Ohtani, E., & Litasov, K. D. (2006). The effect of water on mantle phase transitions. *Water in Nominally Anhydrous Minerals*, *62*, 397–419. https://doi.org/10.2138/rmg.2006.62.17

Olsen, N. (1999a). Induction studies with satellite data. *Surveys in Geophysics*, *20*(3–4), 309–340. https://doi.org/10.1023/a:1006611303582

Olsen, N. (1999b). Long-period (30 days-1 year) electromagnetic sounding and the electrical conductivity of the lower mantle beneath Europe. *Geophysical Journal International*, *138*(1), 179–187. https://doi.org/10.1046/j.1365-246x.1999.00854.x

Panero, W. R., Smyth, J. R., Pigott, J. S., Liu, Z. X., & Frost, D. J. (2013). Hydrous ringwoodite to 5 K and 35 GPa: Multiple hydrogen bonding sites resolved with FTIR spectroscopy. *American Mineralogist*, *98*(4), 637–642. https://doi.org/10.2138/am.2013.3978

Peng, Y., & Deng, J. (2023). Hydrogen diffusion in the lower mantle revealed by machine learning potentials [Dataset]. *OSF*. https://doi.org/10.17605/OSF.IO/BRWCV

Peng, Y., & Deng, J. (2024). Thermal conductivity of $MgSiO_3$-H_2O system determined by machine learning potentials. *Geophysical Research Letters*, *51*(5), e2023GL107245. https://doi.org/10.1029/2023GL107245

Perdew, J. P., Ruzsinszky, A., Csonka, G. I., Vydrov, O. A., Scuseria, G. E., Constantin, L. A., et al. (2008). Restoring the density-gradient expansion for exchange in solids and surfaces. *Physical Review Letters*, *100*(13), 4. https://doi.org/10.1103/PhysRevLett.100.136406

Piaggi, P. M., & Parrinello, M. (2019). Multithermal-multibaric molecular simulations from a variational principle. *Physical Review Letters*, *122*(5), 6. https://doi.org/10.1103/PhysRevLett.122.050601

Plimpton, S. (1995). Fast parallel algorithms for short-range molecular-dynamics. *Journal of Computational Physics*, *117*(1), 1–19. https://doi.org/10.1006/jcph.1995.1039

Plimpton, S., Kohlmeyer, A., Thompson, A., Moore, S., & Berger, R. (2021). LAMMPS stable release 29 September 2021 [Software]. *Zenodo*. https://doi.org/10.5281/zenodo.6386596

Puthe, C., Kuvshinov, A., Khan, A., & Olsen, N. (2015). A new model of Earth's radial conductivity structure derived from over 10 yr of satellite and observatory magnetic data. *Geophysical Journal International*, *203*(3), 1864–1872. https://doi.org/10.1093/gji/ggv407

Schmalzried, H., & Schmalzried, H. (1974). *Solid state reactions*. Verl. Chemie.

Scipioni, R., Stixrude, L., & Desjarlais, M. P. (2017). Electrical conductivity of SiO_2 at extreme conditions and planetary dynamos. *Proceedings of the National Academy of Sciences of the United States of America*, *114*(34), 9009–9013. https://doi.org/10.1073/pnas.1704762114

Shankland, T. J., Peyronneau, J., & Poirier, J. P. (1993). Electrical-conductivity of the Earths lower mantle. *Nature*, *366*(6454), 453–455. https://doi.org/10.1038/366453a0

Shelyapina, M. G. (2022). Hydrogen diffusion on, into and in magnesium probed by DFT: A review. *Hydrogen*, *3*(3), 285–302. https://doi.org/10.3390/hydrogen3030017

Sinmyo, R., Pesce, G., Greenberg, E., McCammon, C., & Dubrovinsky, L. (2014). Lower mantle electrical conductivity based on measurements of Al, Fe-bearing perovskite under lower mantle conditions. *Earth and Planetary Science Letters*, *393*, 165–172. https://doi.org/10.1016/j.epsl.2014.02.049

Slater, J. C. (1964). Atomic radii in crystals. *Journal of Chemical Physics*, *41*(10), 3199–3204. https://doi.org/10.1063/1.1725697

Sun, W., Yoshino, T., Sakamoto, N., & Yurimoto, H. (2015). Hydrogen self-diffusivity in single crystal ringwoodite: Implications for water content and distribution in the mantle transition zone. *Geophysical Research Letters*, *42*(16), 6582–6589. https://doi.org/10.1002/2015gl064486

Tarits, P., & Mandea, M. (2010). The heterogeneous electrical conductivity structure of the lower mantle. *Physics of the Earth and Planetary Interiors*, *183*(1–2), 115–125. https://doi.org/10.1016/j.pepi.2010.08.002

Townsend, J. P., Tsuchiya, J., Bina, C. R., & Jacobsen, S. D. (2016). Water partitioning between bridgmanite and postperovskite in the lowermost mantle. *Earth and Planetary Science Letters*, *454*, 20–27. https://doi.org/10.1016/j.epsl.2016.08.009

Tribello, G. A., Bonomi, M., Branduardi, D., Camilloni, C., & Bussi, G. (2014). PLUMED 2: New feathers for an old bird. *Computer Physics Communications*, *185*(2), 604–613. https://doi.org/10.1016/j.cpc.2013.09.018

Velimsky, J. (2010). Electrical conductivity in the lower mantle: Constraints from CHAMP satellite data by time-domain EM induction modelling. *Physics of the Earth and Planetary Interiors*, *180*(3–4), 111–117. https://doi.org/10.1016/j.pepi.2010.02.007

Verhoeven, O., Thebault, E., Saturnino, D., Houliez, A., & Langlais, B. (2021). Electrical conductivity and temperature of the Earth's mantle inferred from Bayesian inversion of Swarm vector magnetic data. *Physics of the Earth and Planetary Interiors*, *314*, 11. https://doi.org/10.1016/j.pepi.2021.106702

Wang, H., Zhang, L. F., Han, J. Q., & E, W. N. (2018). DeePMD-kit: A deep learning package for many-body potential energy representation and molecular dynamics. *Computer Physics Communications*, *228*, 178–184. https://doi.org/10.1016/j.cpc.2018.03.016

Xu, J., Yamazaki, D., Katsura, T., Wu, X., Remmert, P., Yurimoto, H., & Chakraborty, S. (2011). Silicon and magnesium diffusion in a single crystal of $MgSiO3$ perovskite. *Journal of Geophysical Research: Solid Earth*, *116*(B12), B12205. https://doi.org/10.1029/2011JB008444

Xu, Y. S., McCammon, C., & Poe, B. T. (1998). The effect of alumina on the electrical conductivity of silicate perovskite. *Science*, *282*(5390), 922–924. https://doi.org/10.1126/science.282.5390.922

Yang, M., Karmakar, T., & Parrinello, M. (2021). Liquid-liquid critical point in phosphorus. *Physical Review Letters*, *127*(080603), 080603. https://doi.org/10.1103/PhysRevLett.127.080603

Yang, Y.-N., Du, Z., Lu, W., Qi, Y., Zhang, Y.-Q., Zhang, W.-F., & Zhang, P.-F. (2023). NanoSIMS analysis of water content in bridgmanite at the micron scale: An experimental approach to probe water in Earth's deep mantle. *Frontiers in Chemistry*, *11*. https://doi.org/10.3389/fchem.2023.1166593

Yao, H., Ren, Z., Pan, K., Tang, J., & Zhang, K. (2023). A global mantle conductivity model derived from 8 years of Swarm satellite magnetic data. *Earth and Planetary Physics*, *7*(1), 49–56. https://doi.org/10.26464/epp2023011

Yao, H., Ren, Z., Tang, J., Guo, R., & Yan, J. (2023). Trans-dimensional Bayesian joint inversion of magnetotelluric and geomagnetic depth sounding responses to constrain mantle electrical discontinuities. *Geophysical Journal International*, *233*(3), 1821–1846. https://doi.org/10.1093/gji/ggad029

Yeh, I. C., & Hummer, G. (2004). System-size dependence of diffusion coefficients and viscosities from molecular dynamics simulations with periodic boundary conditions. *Journal of Physical Chemistry B*, *108*(40), 15873–15879. https://doi.org/10.1021/jp0477147

Yoshino, T. (2010). Laboratory electrical conductivity measurement of mantle minerals. *Surveys in Geophysics*, *31*(2), 163–206. https://doi.org/10.1007/s10712-009-9084-0

Yoshino, T., Kamada, S., Zhao, C. C., Ohtani, E., & Hirao, N. (2016). Electrical conductivity model of Al-bearing bridgmanite with implications for the electrical structure of the Earth's lower mantle. *Earth and Planetary Science Letters*, *434*, 208–219. https://doi.org/10.1016/j.epsl.2015.11.032

Zhang, L. F., Han, J. Q., Wang, H., Car, R., & Weinan, E. (2018). Deep potential molecular dynamics: A scalable model with the accuracy of quantum mechanics. *Physical Review Letters*, *120*(14), 6. https://doi.org/10.1103/PhysRevLett.120.143001

Zhou, W. Y., Hao, M., Zhang, J. S., Chen, B., Wang, R. J., & Schmandt, B. (2022). Constraining composition and temperature variations in the mantle transition zone. *Nature Communications*, *13*(1), 9. https://doi.org/10.1038/s41467-022-28709-7

References From the Supporting Information

Bader, R. F. W. (1990). *Atoms in molecules: A quantum theory*. Oxford University Press. https://doi.org/10.1093/oso/9780198551683.001.0001

Bork, N., Bonanos, N., Rossmeisl, J., & Vegge, T. (2011). Ab initio charge analysis of 156 pure and hydrogenated perovskites. *Journal of Applied Physics*, *109*(3), 033702. https://doi.org/10.1063/1.3536484

Fonseca Guerra, C., Handgraaf, J.-W., Baerends, E. J., & Bickelhaupt, F. M. (2004). Voronoi deformation density (VDD) charges: Assessment of the Mulliken, Bader, Hirshfeld, Weinhold, and VDD methods for charge analysis. *Journal of Computational Chemistry*, *25*(2), 189–210. https://doi.org/10.1002/jcc.10351

Hirel, P. (2015). Atomsk: A tool for manipulating and converting atomic data files. *Computer Physics Communications*, *197*, 212–219. https://doi.org/10.1016/j.cpc.2015.07.012

Hirshfeld, F. L. (1977). Bonded-atom fragments for describing molecular charge densities. *Theoretica chimica acta*, *44*(2), 129–138. https://doi.org/10.1007/BF00549096

Jinnouchi, R., Karsai, F., & Kresse, G. (2019). On-the-fly machine learning force field generation: Application to melting points. *Physical Review B*, *100*(1), 014105. https://doi.org/10.1103/PhysRevB.100

Jinnouchi, R., Lahnsteiner, J., Karsai, F., Kresse, G., & Bokdam, M. (2019). Phase transitions of hybrid perovskites simulated by machine-learning force fields trained on the fly with Bayesian inference. *Physical Review Letters*, *122*(22), 225701. https://doi.org/10.1103/PhysRevLett.122.225701

Mulliken, R. S. (1955). Electronic population analysis on LCAO–MO molecular wave functions. I. *The Journal of Chemical Physics*, *23*(10), 1833–1840. https://doi.org/10.1063/1.1740588

Reed, A. E., Weinstock, R. B., & Weinhold, F. (1985). Natural population analysis. *The Journal of Chemical Physics*, *83*(2), 735–746. https://doi.org/10.1063/1.449486

Sanville, E., Kenny, S. D., Smith, R., & Henkelman, G. (2007). Improved grid-based algorithm for Bader charge allocation. *Journal of Computational Chemistry*, *28*(5), 899–908. https://doi.org/10.1002/jcc.20575

Wang, A., Kingsbury, R., McDermott, M., Horton, M., Jain, A., Ong, S. P., et al. (2021). A framework for quantifying uncertainty in DFT energy corrections. *Scientific Reports*, *11*(1), 15496. https://doi.org/10.1038/s41598-021-94550-5